To the Graduate Council:

I am submitting herewith a thesis written by Conrad J. Simon, III entitled "Experimental Study of the Effects of Annealing Time, Equilibrium Angle, and Absolute Misorientation Angle on Thermal Grain-Boundary Grooving in Cube-Textured Nickel." I have examined the final copy of this thesis for form and content and recommend that it be accepted in partial fulfillment of the requirements for the degree of Master of Science, with a major in Metallurgical Engineering.

Mary Helen McCay

Mary Helen McCay, Major Professor

We have read this thesis
and recommend its acceptance:

John O Hopkins

David C Joy

Accepted for the Council:

Associate Vice Chancellor and
Dean of the Graduate School

Experimental Study of the Effects of Annealing Time, Equilibrium Angle, and Absolute Misorientation Angle on Thermal Grain-Boundary Grooving in Cube-Textured Nickel

A Thesis
Presented for the
Master of Science
Degree
The University of Tennessee, Knoxville

Conrad J. Simon, III
May 1999

ACKNOWLEDGEMENTS

The author would like to thank his graduate committee members, Dr. Mary Helen McCay, Dr. John A. Hopkins, and Dr. David C. Joy for their valuable advice and support. In addition, I would like to thank the members of the Superconducting Materials Group at Oak Ridge National Laboratory for the use of their facilities and for their friendly assistance and guidance during the course of my research. In particular, I thank Dr. Amit Goyal and Dr. Robert Williams for their time, patience, and direction. I am grateful to The University of Tennessee Space Institute and the Department of Energy for funding this research.

ABSTRACT

Several technical problems are associated with the rolling-assisted biaxially-textured substrates (RABiTS) method of fabricating long lengths of high-temperature superconducting wire. For example, controlling or eliminating thermal grain-boundary groove defects on the Ni base layer of the substrate is an important concern. Thermal grooves on the surface of the Ni may have the potential to cause cracks or growth defects to form in the buffer and superconducting layers which are epitaxially deposited on the Ni. Thus, the effects of annealing time, equilibrium angle, and absolute misorientation angle on thermal grain-boundary grooving in cube-textured nickel were investigated.

Small samples of RABiTS Ni were recrystallized at 800°C for times of 10, 30, 60, and 120 minutes to produce diffusion-induced thermal grooves on their surfaces. The linear dimensions and equilibrium angles these grooves were measured using atomic force microscopy. The misorientations of grains at triple point junctions were measured using electron back-scatter diffraction, and the cube-texture of the samples was analyzed with x-ray diffraction. Grain size measurements were also made on each sample.

The linear dimensions of grooves evolved with annealing time in accordance with Mullins' theory of thermal grooving. Average groove depths increased with increasing equilibrium angle; however, there was only a slight tendency for groove depth to increase with increasing absolute misorientation angle. In general, groove depths did not exceed 650 Å. The cube texture and grain size of the samples were typical of RABiTS Ni.

TABLE OF CONTENTS

CHAPTER		PAGE
1.	INTRODUCTION	1
	1.1 General Background	1
	1.2 Statement of the Problem	4
	1.3 Objectives and Approach	6
2.	BACKGROUND AND LITERATURE REVIEW	7
	2.1 YBCO Superconducting Wire	7
	2.2 Rolling-Assisted Biaxially-Textured Substrates (RABiTS)	8
	2.3 Thermally Activated Grain-Boundary Grooving	12
	2.4 Grain-Boundary Misorientation	22
3.	EXPERIMENTAL PROCEDURE	26
	3.1 Material	26
	3.2 Sample Preparation	26
	3.3 AFM Measurements	29
	3.4 EBSD Analysis	35
	3.5 X-ray Diffraction Analysis	37
	3.6 Grain Size Measurements	38
4.	RESULTS AND DISCUSSION	39
	4.1 Qualitative Observations of Thermal Grooving in Cube-Textured Ni	39
	4.2 Effect of Annealing Time on Thermal Groove Dimensions	45
	4.3 Effect of Equilibrium Angle on Groove Depth	53
	4.4 Effect of Absolute Misorientation Angle on Groove Depth	56
	4.5 Texture Analysis	62
	4.6 Grain Size and Growth	62
5.	CONCLUSIONS	69
LIST OF REFERENCES		72
APPENDIX - EXPERIMENTAL ERROR		76
VITA		82

LIST OF FIGURES

FIGURE		PAGE
1.1.	Diagram of the oxide-powder-in-tube (OPIT) process	3
1.2.	Diagram of the rolling-assisted biaxially-textured substrates (RABiTS) process	3
1.3.	Scanning electron micrograph of a YBCO layer deposited on a YSZ/CeO_2/Ni, RABiTS architecture	5
2.1.	(111) and (200) x-ray pole figures showing a copper-type texture in 99.99% Ni sheet after rolling to > 90% reduction	10
2.2.	Schematic diagram of cube texture in a metal sheet	11
2.3.	Cross-sectional schematics of four RABiT multilayer structures	11
2.4.	Diagram of a symmetrical, thermal grain-boundary groove showing the balance of surface energies at the boundary	13
2.5.	Relative grain-boundary energy as a function of misorientation angle for [001] tilt boundaries at 1065°C	15
2.6.	Profiles of thermal grain-boundary grooves formed by (a) evaporation-condensation and (b) surface diffusion	15
2.7.	Groove profiles plotted for numerical solutions (solid line) compared with the solutions of Mullins (dotted line) for the "small-slope" approximation	18
2.8.	Comparison of Mullins' kinetic laws (solid lines) with the numerical solutions of Zhang and Schneibel (symbols)	20
2.9.	Diagram of boundary anchoring at a V-notch	21
2.10.	Schematic illustrations of a (a) tilt boundary and (b) a twist boundary	23
2.11.	Illustrations of the Euler angle rotations which describe the final orientation of a crystal coordinate system K_B with respect to the sample coordinate system K_A	25

3.1. Typical recrystallization annealing cycle for RABiTS Ni 28

3.2. Diagram of the nanoindentation grid used to locate grain-boundary triple points 30

3.3. SEM micrograph of four nanoindentations in RABiTS Ni, forming one element of the array shown in Figure 3.2. 30

3.4. Calibration plot for the Park Scientific AutoProbe XL showing the deviation of the z-piezo response from linearity 33

3.5. Illustrations showing various measurements which were made from AFM images of triple points 36

4.1. AFM scan of diffusion-induced thermal grooves at a triple point in cube-textured Ni 40

4.2. Photomicrograph of diffusion-induced, thermal grain-boundary grooves on the surface of cube-textured Ni 41

4.3. AFM scan of faceted thermal grooves at a triple point in cube-textured Ni .. 43

4.4. Distributions of grain-boundary groove, average widths in cube-textured nickel 46

4.5. Distributions of grain-boundary groove, average depths in cube-textured nickel 48

4.6. Average width of thermal grooves as a function of time for cube-textured nickel annealed at 800°C 51

4.7. Average depth of thermal grooves as a function of time for cube-textured nickel annealed at 800°C 52

4.8. Average depth of thermal grooves as a function of equilibrium angle for cube-textured nickel 54

4.9. Instantaneous growth rates of thermal grooves for four times at 800°C as a function of slope m and equilibrium angle α 57

4.10. SEM image of the triple point shown in Figure 4.1. 58

4.11. Plots of average groove depth versus absolute misorientation angle for cube-textured nickel 60

4.12. (111) x-ray diffraction pole figures for RABiTS nickel after recrystallization, indicating the presence of a sharp {100}⟨001⟩ cube texture 63

4.13. Photomicrographs of the grain structure of RABiTS Ni samples after recrystallization 66

A.1. Schematic diagram of measurement error due to the finite diameter of an AFM probe tip 79

NOMENCLATURE

a	coefficient in an equation for fitting a curve to groove width data
A	coefficient in Mullins' kinetic law for calculating the depth of a condensation-evaporation groove
b	coefficient in an equation for fitting a curve to groove depth data
B	coefficient in Mullins' kinetic law for calculating the depth of a diffusion induced groove
d	groove depth
d'	instantaneous groove growth rate
d_{avg}	average grain diameter
D_s	coefficient of surface diffusion
g	rotation matrix
$g1$	absolute orientation of a grain in a polycrystalline material (grain 1)
$g2$	absolute orientation of a grain in a polycrystalline material (grain 2)
$g12$	matrix describing the misorientation between grains 1 and 2
J_c	critical current density
k	Boltzmann's constant
K_A	specimen coordinate system
K_B	crystal coordinate system
K_{IC}	fracture toughness
m	slope of the free surface at the groove root
M	weight of a molecule

p_o	vapor pressure in equilibrium with a plane surface
R	correlation coefficient
t	time
T	temperature
T_c	critical temperature
w	groove width
x	width; x-axis in the specimen coordinate system; time
x'	x-axis in the crystal coordinate system
y	length; groove width; groove depth; y-axis in the specimen coordinate system
y'	y-axis in the crystal coordinate system
z	height; z-axis in the specimen coordinate system
z'	z-axis in the crystal coordinate system
α	equilibrium angle at the groove root
γ_b	grain-boundary energy
γ_{sv}	solid-vapor interfacial (free surface) energy
θ	dihedral angle formed at the groove root
θ_o	angle between the grain-boundary plane and the perpendicular to the surface of the sample
ν	number of atoms per unit area
ϕ	Euler angle describing the rotation about crystal x' axis
ϕ_1	Euler angle describing the first rotation about the z' axis
ϕ_2	Euler angle describing the second rotation about the z' axis

ω	misorientation angle between two grains in a polycrystalline material
Ω	molecular volume

Abbreviations

AFM	Atomic Force Microscope
Bi - 2223	Bismuth Strontium Calcium Copper Oxide
EBSD	Electron Back-Scatter Diffraction
HTS	High-Temperature Superconductor
IBAD	Ion-Beam-Assisted Deposition
OIM	Orientation Image Microscopy
OPIT	Oxide-Powder-In-Tube
ORNL	Oak Ridge National Laboratory
PSI	Park Scientific Instruments
RABiTS	Rolling-Assisted Biaxially-Textured Substrates
SEM	Scanning Electron Microscope
SIT	Silicon Intensified Target
YBCO	Yttrium Barium Copper Oxide
YSZ	Yttria-Stabilized Zirconia

CHAPTER 1

INTRODUCTION

1.1 General Background

Superconductivity is a phenomenon characterized by the sudden disappearance of all electrical resistance in a material at an exact temperature called the critical temperature T_c.[1] It was discovered by Kamerlingh-Onnes in 1911 when he observed that mercury conducted electrical current without resistance at a temperature of 4.2 K.[1] For almost seventy-five years following this discovery, applications involving superconductors were confined to very low temperatures near or at the boiling point of liquid helium (4.2 K) because of their low critical temperatures ($T_c < 23$ K).

A new class of superconducting materials with comparatively high transition temperatures was discovered by A. Bednorz and K.A. Müller (IBM, Zurich) in 1986.[1,2] These high-temperature superconductors (HTSs) are based on copper oxide compounds and have T_c's ranging from approximately 38 K to 135 K. In fact, several of these compounds remain superconducting near 100 K. One important compound, yttrium barium copper oxide (YBCO), which is the subject of extensive research, superconducts up to 92 K.[2] Because YBCO has a transition temperature above 77 K, liquid nitrogen can be used to cool it into the superconducting state. This is of great economic significance because liquid nitrogen is fifty times less expensive than the liquid helium which is used to

cool low-temperature superconductors.[3] Although the copper oxide superconductors with T_c's above 77 K bring superconductivity into the realm of practical applications, the fabrication of these materials into useful conductors has proven to be challenging.

Two types of superconducting wire which have gained particular interest among researchers are oxide-powder-in-tube (OPIT) tapes[3-5] and coated conductors utilizing rolling-assisted biaxially-textured substrates (RABiTS). The OPIT process (Figure 1.1) consists of filling a silver tube with an oxide precursor powder, "thermomechanically" drawing and rolling the tube into the desired shape, and heat treating the wire to produce the superconductor from the precursor.[5] Bismuth strontium calcium copper oxide (Bi-2223), OPIT, superconducting tapes have transport critical current densities J_c's of approximately 10-30 x 10^3 A/cm^2 at 77 K in self-field.[5] The critical current density is the maximum current density that a superconductor can sustain without becoming nonsuperconducting. The RABiTS process (Figure 1.2), which was pioneered by researchers at the Oak Ridge National Laboratory (ORNL), uses "thermomechanical processes" to obtain a strong, biaxial texture (preferred grain orientation) in a base metal such as Ni.[5-8] Next, appropriate chemical and structural buffer layers, such as CeO_2 and yttria-stabilized zirconia (YSZ), are epitaxially deposited on the base metal. Lastly, a superconducting layer (usually YBCO) is epitaxially deposited on the completed RABiT substrate. YBCO superconducting tapes produced by the RABiTS technique have J_c's of approximately 10^6 A/cm^2, 77 K, 0 T.[7-9]

Because of its high T_c (92 K) and ability to carry a supercurrent in large magnetic fields, YBCO is one of the most desirable copper oxide materials for HTS wire

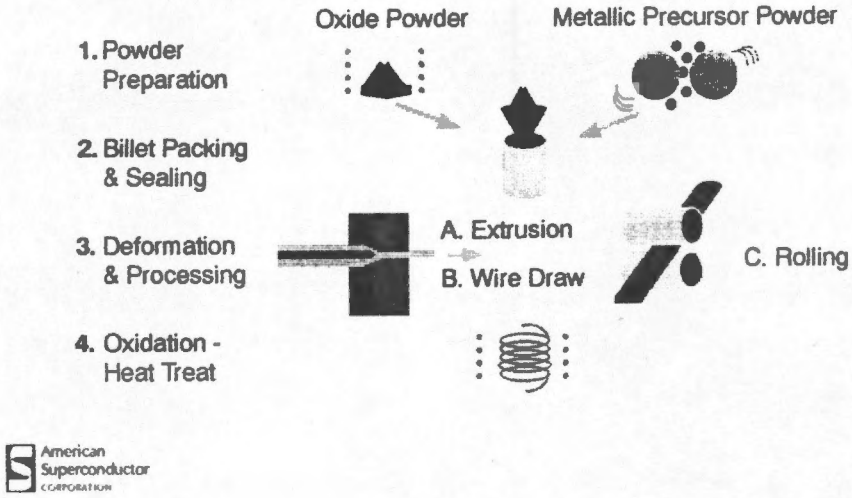

Figure 1.1. Diagram of the oxide-powder-in-tube (OPIT) process.

Source: T.P. Sheahen, *Introduction to High-Temperature Superconductivity* (Plenum Press, New York, 1994).

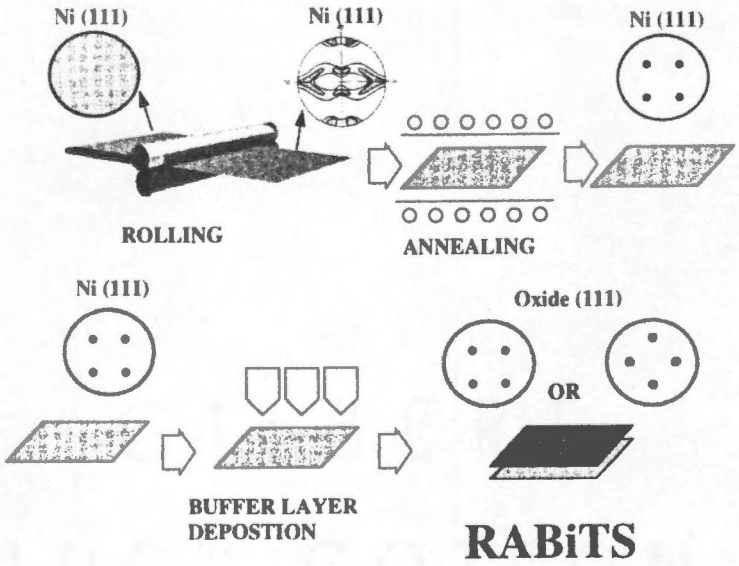

Figure 1.2. Diagram of the rolling-assisted biaxially-textured substrates (RABiTS) process.

Source: A. Goyal, D. P. Norton, D. K. Christen, E. D. Specht, M. Paranthaman, D. M. Kroeger, J. D. Budai, Q. He, F. A. List, R. Feenstra, H. R. Kerchner, D. F. Lee, E. Hatfield, P. M. Martin, J. Mathis, and C. Park, *Appl. Supercond.* **4**, 403 (1998).

fabrication. Unfortunately, problems with brittleness and weak links have made it difficult to manufacture long lengths of YBCO superconducting wire.

The fracture toughness K_{IC} of YBCO is reported to be 1.8 MPa$\sqrt{m}$, compared to 50 MPa$\sqrt{m}$ for steel.[2] Fracture toughness is a material property which characterizes the resistance of a material to crack propagation and fracture.[10,11] The low fracture toughness of YBCO indicates that it is very brittle.

Weak links can severely degrade the J_c of YBCO. A weak link is essentially a nonsuperconducting region, such as a high-angle grain boundary, within a superconductor that severely attenuates the supercurrent tunneling through it.[2] Researchers have shown that long-range conduction in a polycrystalline superconductor occurs by the percolation of current through a continuous network of low-angle grain boundaries.[12-14] Thus, it is important to reduce the number of high-angle grain boundaries in YBCO to promote percolation. Fortunately, the development of RABiTS has addressed the problem of weak links; however, the problem of brittleness remains.

1.2 Statement of the Problem

Microscopic examinations of HTS coated conductors based on RABiTS sometimes reveal cracks in the YBCO layer and/or the buffer layers. Furthermore, extensive networks of thermally grooved grain boundaries have been observed in the Ni layer of RABiTS after annealing at 800°C. Occasionally, cracks and/or discontinuities in the YBCO layer appear to follow grain boundaries in the Ni layer for short distances (Figure 1.3).[15] Also, spurious growths of buffer layer material can originate at the

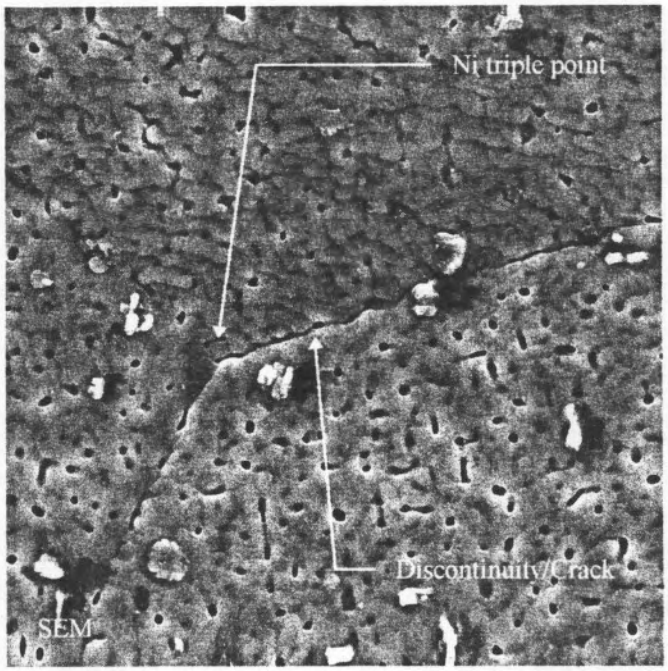

Figure 1.3. Scanning electron micrograph of a YBCO layer deposited on a YSZ/CeO_2/Ni, RABiTS architecture. Cracks/discontinuities in the YBCO layer follow nickel grain boundaries.

Source: D. F. Lee (private communication).

grooves during deposition. Clearly, cracks, discontinuities, or spurious growths originating at thermal grooves in the Ni layer and propagating to the superconducting layer would be detrimental to the physical and mechanical performance of the YBCO. The axial, bending, and torsional loads that superconducting tapes will encounter during preparation, handling, and service could worsen the problems caused by such features.

1.3 Objectives and Approach

The main objectives of the research presented in this thesis were: (1) to determine the effects of annealing time, equilibrium angle, and absolute misorientation angle of RABiTS nickel grains on thermal grooving at 800°C and (2) to characterize thermally grooved grain boundaries in RABiTS nickel in order to determine their significance as material defects. Also, the effects of annealing time on the formation of cube texture and Ni grain size were investigated. By utilizing the results of this research, the processing of RABiTS Ni may be modified to eliminate or minimize the formation of thermal grain-boundary grooves.

Atomic force microscopy (AFM) was used to determine the size and geometry of Ni grain-boundary grooves after annealing at 800°C for times of 10, 30, 60, and 120 minutes. Electron back-scatter diffraction (EBSD) was used to measure the absolute misorientation of Ni grains at triple points previously examined with the AFM. The sharpness of the cube texture in these samples was evaluated by generating x-ray diffraction pole figures. Grain size measurements were made from optical micrographs of the annealed Ni samples.

CHAPTER 2

BACKGROUND AND LITERATURE REVIEW

2.1 YBCO Superconducting Wire

Since its debut in 1987, researchers have made several attempts by various techniques to produce a high critical current density superconducting wire using yttrium barium copper oxide (YBCO). Of the methods tried, only a few have been successful. For example, the OPIT process, which is used to make Bi-2223 conductors, does not work with YBCO because it results in a polycrystalline superconductor with poor grain alignment and a large population of high-angle grain boundaries, which can behave as weak links.[2] In fact, Dimos *et al.*[16] have shown with bicrystal experiments that the J_c of YBCO is strongly dependent on grain-boundary misorientation angle. They discovered that grain boundaries with misorientation angles exceeding 10° were weak links. Thus, the success of any method used to make high-J_c, polycrystalline, YBCO superconducting tapes depends on its ability to produce a high degree of in-plane and out-of-plane grain alignment in the superconductor.[16] Two methods, ion-beam-assisted deposition (IBAD)[17,18] and epitaxial deposition on rolling-assisted biaxially-textured substrates (RABiTS), have successfully produced short lengths of high-J_c YBCO tapes. In this study, only the RABiTS method is of interest.

2.2 Rolling-Assisted Biaxially-Textured Substrates (RABiTS)

Recent work at the Oak Ridge National Laboratory has yielded a potential method for producing high critical current density YBCO superconducting wires. The technique, known as RABiTS, involves the use of "industrially scaleable, thermomechanical processes" to produce long lengths of smooth, flexible, cube-textured substrates of Ni or Cu.[5-8] Chemical and structural buffer layers, which may be noble metals such as Pd, Pt, and Ag or oxides such as CeO_2 and YSZ, are deposited on the textured base metal (see Figure 1.2).[5-9,19] The YBCO superconductor is deposited on top of this multilayer substrate system.

Rolling-assisted biaxially-textured substrates were developed to serve four critical functions as related to the fabrication of YBCO superconducting wire. First, the metal substrate provides the mechanical strength required of the wire. The superconductor is far to weak and brittle to support itself in the form of a film. Secondly, the epitaxial deposition of the superconductor on a sharply cube-textured metallic substrate minimizes weak links by greatly reducing the number of high-angle grain boundaries formed during growth.[5-8] Thirdly, the buffer layers grown on the metallic substrate serve to reduce the atomic lattice mismatch between the metal and the superconductor and thus reduce the stress induced during deposition.[9,19] Lastly, RABiTS acts as a barrier to prevent Ni atoms from diffusing into the YBCO.[9,19] This is important because Ni will substitute for Cu in the superconductor and degrade its superconductive properties. Ni is most commonly chosen as the foundation of a RABiT substrate because it is more resistant to oxidation

than Cu, and it easily develops the {100}⟨001⟩ cube texture necessary for the subsequent deposition of buffer layers and YBCO.[6,9,19]

Producing biaxially-textured Ni substrates essentially consists of two major steps. First, a polycrystalline rod of Ni (99.99% pure) with a random grain orientation is cold-rolled to more than 90% deformation to form a 125 μm thick tape.[5-9,19,20] Goyal *et al.*[6] and Makita *et al.*[21] have shown that a copper-type rolling texture is formed in Ni that is subjected to such large reductions. Figure 2.1 (a and b) shows (111) and (200) x-ray pole figures which indicate this rolling texture in as-rolled, high purity Ni. The copper-type rolling texture, which is dependent on the amount and type of reduction,[10,22] is essential to the complete formation of the desired cube texture during the next step, recrystallization. This is accomplished by annealing the Ni in the temperature range of 400 to 1000°C. After recrystallization, the grain diameter and the thickness of the tape are usually about the same (~ 125 μm).[5-8] Figure 2.1 (c and d) shows (111) and (200) x-ray pole figures for recrystallized Ni which was annealed for 4 hours at 1000°C in a high vacuum.[6] A sheet or thin tape of fcc metal with a refined cube texture as shown in Figure 2.1 (c and d) is practically a single crystal because the cube axes of the grains are highly aligned with the rolling, transverse, and normal directions of the tape[23,24] (Figure 2.2).

Following the preparation of the biaxially-textured Ni, metallic and/or ceramic buffer layers are deposited. Figure 2.3 shows RABiTS architectures developed at ORNL that employ several different buffer layer systems. These epitaxially deposited intermediate layers are expected to transfer the biaxial texture of the Ni to the superconductor. One commonly used buffer layer combination is that of CeO_2 and YSZ.

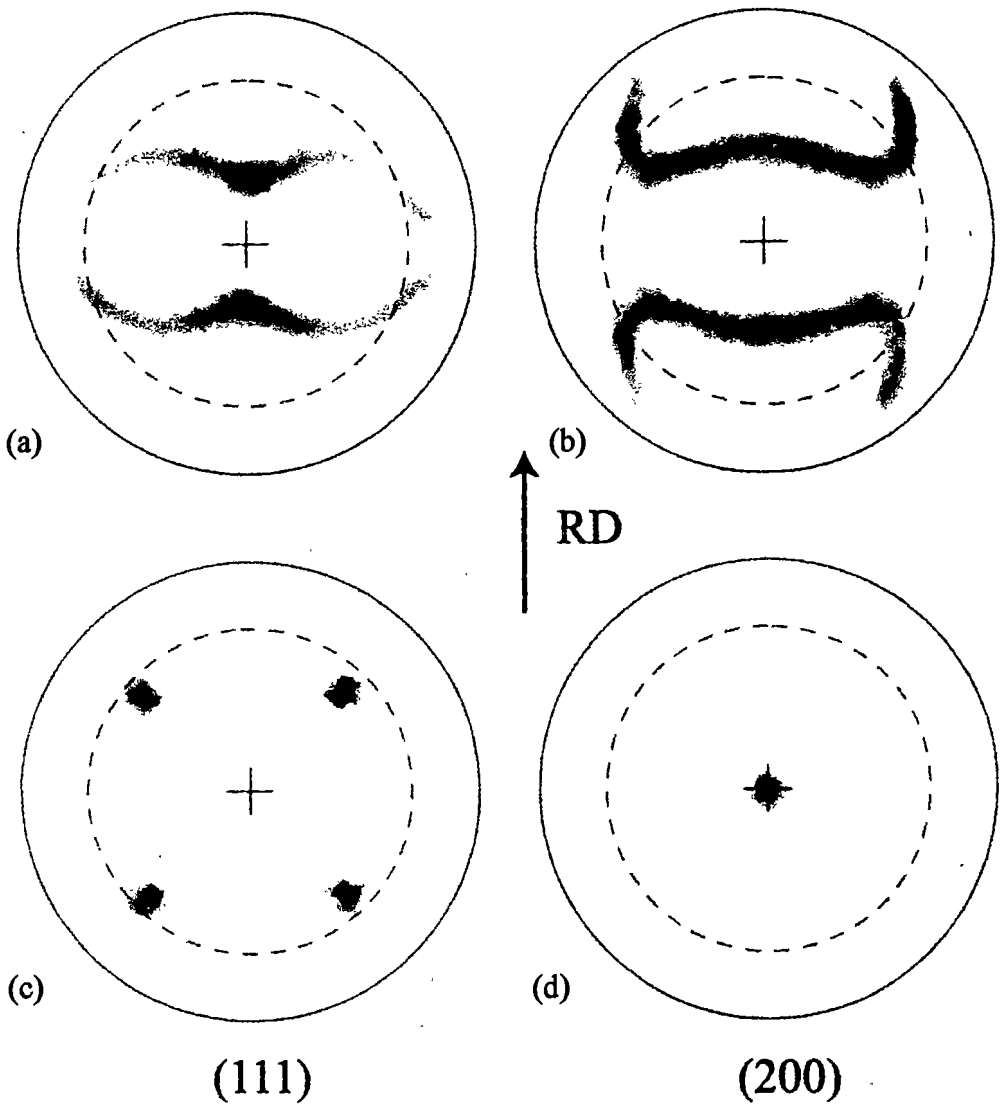

Figure 2.1. (a and b) (111) and (200) x-ray pole figures showing a copper-type texture in 99.99% Ni sheet after rolling to > 90% reduction. (c and d) (111) and (200) x-ray pole figures for the same sheet after recrystallization at 1000°C for 4 hr. showing the development of a strong cube texture.

Source: A. Goyal, D. P. Norton, D. K. Christen, E. D. Specht, M. Paranthaman, D. M. Kroeger, J. D. Budai, Q. He, F. A. List, R. Feenstra, H. R. Kerchner, D. F. Lee, E. Hatfield, P. M. Martin, J. Mathis, and C. Park, *Appl. Supercond.* **4**, 403 (1998).

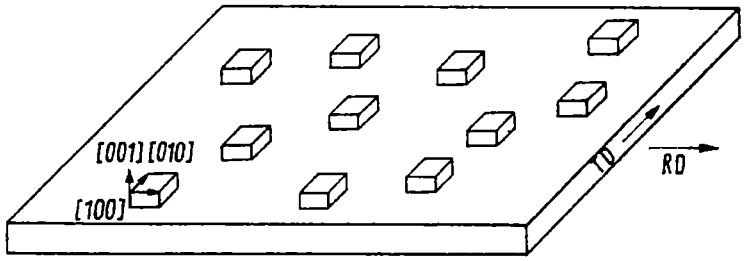

Figure 2.2. Schematic diagram of cube texture in a metal sheet.

Source: H.-J. Bunge, *Texture Analysis in Material Science: Mathematical Methods* (Butterworths, London, 1982).

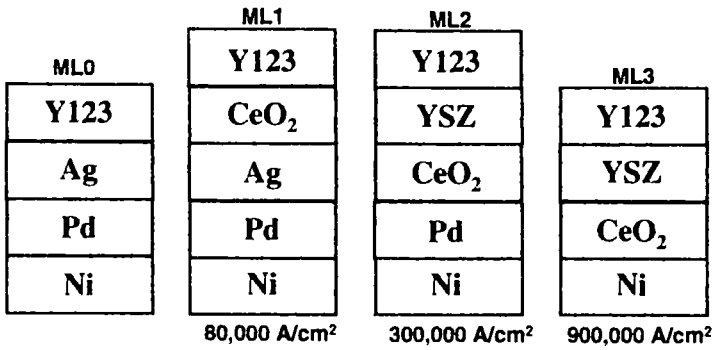

Figure 2.3 Cross-sectional schematics of four RABiT multilayer structures.

Source: A. Goyal, D. P. Norton, D. K. Christen, E. D. Specht, M. Paranthaman, D. M. Kroeger, J. D. Budai, Q. He, F. A. List, R. Feenstra, H. R. Kerchner, D. F. Lee, E. Hatfield, P. M. Martin, J. Mathis, and C. Park, *Appl. Supercond.* 4, 403 (1998).

Such layers, which can be 50 - 4000 Å thick each, are typically deposited by electron beam evaporation or r.f. sputtering, but pulsed laser ablation has also been used.

2.3 Thermally Activated Grain-Boundary Grooving

Because the surface condition of a biaxially-textured Ni substrate can affect the quality of the layers deposited on it, a great interest in surface defects has arisen. One defect which is fairly abundant on the surface of biaxially-textured Ni after recrystallization at 800°C is the thermal grain-boundary groove. In order to help preserve the physical and mechanical properties of the YBCO superconductor, the formation of grain-boundary grooves should be controlled or eliminated. The first step in controlling these grooves is to better understand what factors affect their formation and growth.

Mullins[25,26] recognized that grooves may develop on the surface of a polycrystalline material during high temperature annealing where grain boundaries meet the free surface of the specimen. Surface tension forces, which cause grain boundaries to minimize their free energies by reducing their surface areas, are responsible for the evolution of grooves.[26] Figure 2.4 shows a diagram of a symmetrical groove and depicts the necessary balance of surface energies at the boundary. As discussed in Read-Hill,[27] the balance of the vertical components of the surface energies is given by:

$$\gamma_b = 2\gamma_{sv} \cos\frac{\theta}{2} \tag{2.1}$$

where

γ_b = grain-boundary energy
γ_{sv} = the solid-vapor interfacial (free surface) energy
θ = the dihedral angle formed at the groove root

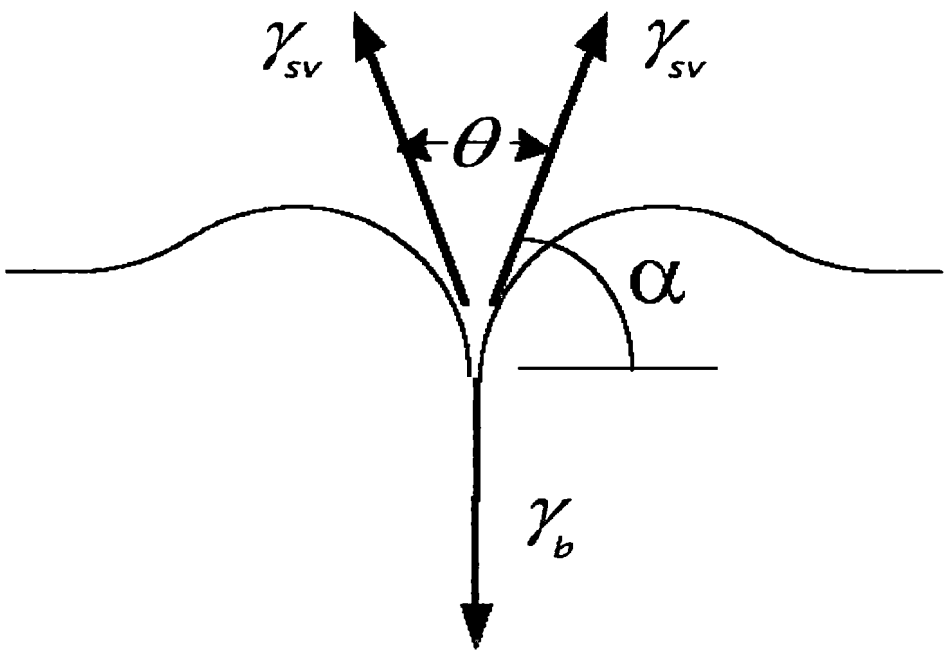

Figure 2.4 Diagram of a symmetrical, thermal grain-boundary groove showing the balance of surface energies at the boundary.

and θ is related to the equilibrium angle α by

$$\theta = 180 - 2\alpha \tag{2.2}$$

In Equation 2.1, the effect of interfacial torques, which tend to rotate grain boundaries into low energy orientations,[28] has been neglected. The omission is permissible because interfacial torques are very small or nonexistent at the symmetrical intersection of a grain boundary and a free surface.[28] Thus, they will not significantly affect the balance of surface tensions at the intersection.

Gjostein and Rhines[29] have shown in their grain-boundary misorientation experiments with copper bicrystals that Equation 2.1 can be used successfully to calculate γ_b from measurements of θ. They also discovered that only symmetrical grooves gave reproducible values of θ. Figure 2.5 shows how relative grain-boundary energy depends on the misorientation angle ω for [001] tilt boundaries in copper.[29]

Mullins[25] developed a theory of thermal grooving and calculated the time-dependent profiles of symmetrical grooves formed by surface diffusion and evaporation-condensation (Figure 2.6). His theory suggests that surface diffusion is dominant during the initial formation of a thermal groove but that its relative importance decreases as the groove grows. Because the equilibrium angle α is quickly formed by the diffusion of atoms in the grain boundary-free surface intersection, curved ridges form on either side of the groove (see Figure 2.4). These convex ridges create curvature gradients which drive the surface diffusion of material. As the ridges level out due to preferential evaporation and/or surface diffusion, the equilibrium angle is disrupted, and the groove deepens to maintain its equilibrium shape.[25]

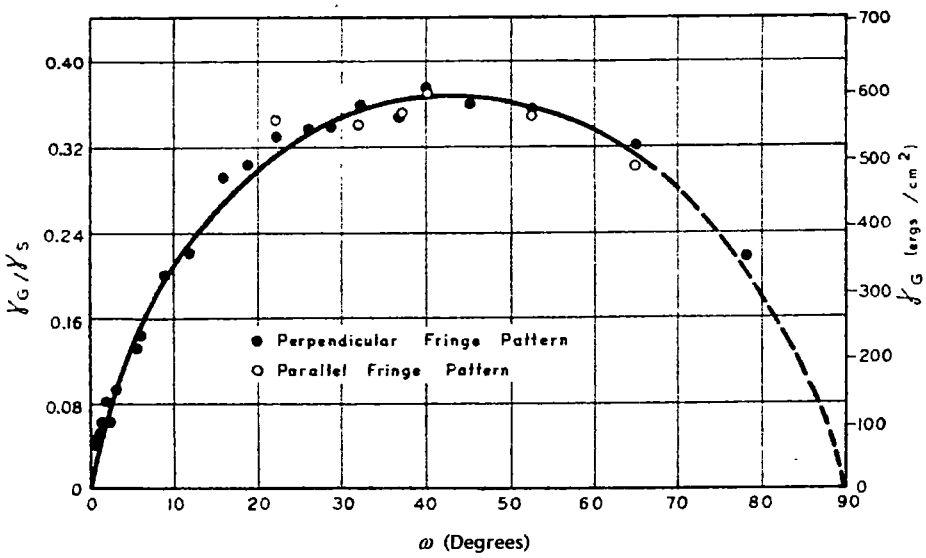

Figure 2.5. Relative grain-boundary energy as a function of misorientation angle for [001] tilt boundaries at 1065°C.

Adapted from N.A. Gjostein and F.N. Rhines, *Acta. Met.* 7, 319 (1959).

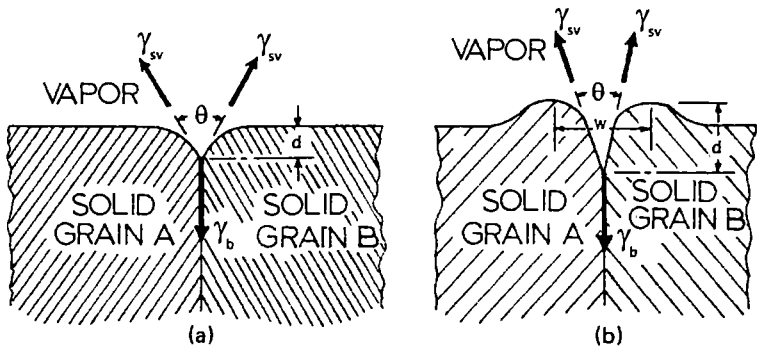

Figure 2.6. Profiles of thermal grain-boundary grooves formed by (a) evaporation-condensation and (b) surface diffusion.

Adapted from L.E. Murr, *Interfacial Phenomena in Metals and Alloys* (Addison-Wesley, Reading, MA, 1975).

In forming his theory of thermal grooving, Mullins arrived at a "closed-form solution" to the curvature-driven, surface-diffusion problem by linearizing his "nonlinear partial differential equation" for describing the development of the surface-diffusion groove profile.[30] His solution is restricted to surfaces which are virtually flat, i.e., where the slope of a groove profile is small.[25,30] From his solution, Mullins derived two "kinetic laws"[30] for calculating the dimensions of a symmetrical grain-boundary groove. The first gives the groove depth *d*, measured with reference to the surface maxima. For a diffusion-induced groove, the relation is:[25]

$$d = 0.973m(Bt)^{\frac{1}{4}} \tag{2.3}$$

where t is time in seconds, m is the slope of the surface at the groove root given by

$$m = \tan \alpha \tag{2.4}$$

and B is defined by

$$B = \frac{D_s \gamma_{sv} \Omega^2 \nu}{kT} \tag{2.5}$$

where

D_s = the coefficient of surface diffusion
γ_{sv} = the surface free energy per surface area
Ω = the molecular volume
ν = the number of atoms per unit area
k = the Boltzmann constant
T = the absolute temperature in K

The second equation yields the width w of a groove, which is measured between the two surface maxima. The width is given by[25]

$$w = 4.6(Bt)^{\frac{1}{4}} \tag{2.6}$$

where B and t have the same definitions as in the equation for depth. As can be seen, the width of a diffusion-induced groove is independent of slope and is thus not related to the dihedral angle. However, both the depth and width of a diffusion-induced groove are proportional to $(Bt)^{\frac{1}{4}}$. Thus, for a specific slope, the shape of a groove is independent of time.[31]

For grooves formed by condensation-evaporation, Mullins showed that the time and slope-dependent groove depth d is given by[25]

$$d = 1.13m(At)^{\frac{1}{2}} \tag{2.7}$$

where t is time in seconds, m is the slope of the groove, and A is defined by

$$A = \frac{p_o \Omega^2 \gamma_{sv}}{(2\pi M)^{\frac{1}{2}} (kT)^{\frac{3}{2}}} \tag{2.8}$$

where p_o is the vapor pressure in equilibrium with a plane surface, and M is the weight of a molecule. The variables Ω, γ_{sv}, k, and T have the same definitions as in Equation 2.5. As with the diffusion-induced groove profile, the shape of the evaporation-condensation groove profile is time-independent.

Zhang and Schneibel[30] developed a numerical solution to "Mullins' 4th order, nonlinear partial differential equation for surface mass transport," and simulated grain-boundary grooving using a computer. They generated profiles of diffusion-induced grooves based on their numerical solution and compared them to profiles generated using Mullins' linearized solution. When the computer was used to numerically evaluate Mullins' analytical solution at small values of Bt, instabilities arose in the profiles that were

generated (Figure 2.7). These instabilities were more severe for a slope $m = 1.0$ than for $m = 0.1$. Zhang and Schneibel attributed this instability to the finite numerical precision of the computer used in their computations. The computer essentially cut off the higher order terms of Mullins' infinite series solution. Despite this problem, Figure 2.8 (a) shows that the solution of Zhang and Schneibel is in excellent agreement with Mullins' solution for calculations of groove depth when groove slopes are small ($m \leq 0.2$). Also, Figure 2.8 (b), shows that groove width is independent of slope.[30] The numerical simulation confirms the validity of Mullins' solution for calculating thermal groove profiles formed by surface diffusion when the grooves have small slopes, and it justifies the use of Equations 2.3 and 2.6 for estimating groove depth and width, respectively.

According to Read-Hill,[27] thermal grooving can affect normal grain growth in a polycrystalline material by pinning grain boundaries. If the average grain size of a polycrystal is small with respect to the specimen thickness, the effect of grooving on grain growth will be negligible. On the other hand, if grains are large, i.e., with a diameter approximately equal to the specimen thickness, the rate of grain growth will probably be reduced by boundary pinning.[27]

Mullins[26] has argued that the pinning of a particular boundary depends on the angle θ_o that the grain boundary plane makes with the perpendicular to the surface of the sample. In Figure 2.9, a thermal groove is depicted as a rigid, fixed "V-notch." If a grain boundary lies in the area between the solid lines *a* and *b* in the diagram, it will be pinned to the groove notch. The boundary cannot move away from the groove because it must lengthen in the process, increasing its free energy. This is not thermodynamically

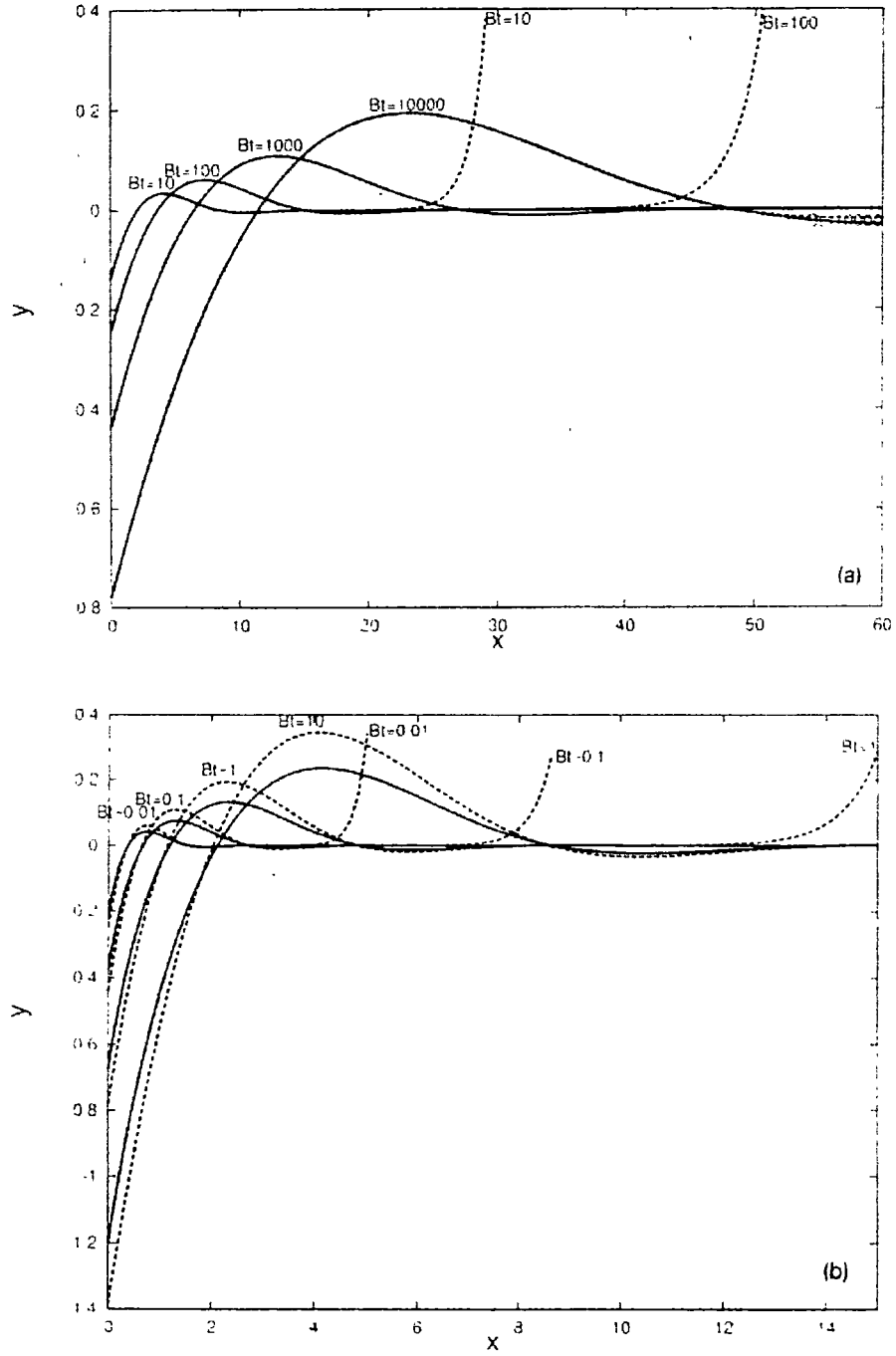

Figure 2.7. Groove profiles plotted for numerical solutions (solid line) compared with the solutions of Mullins (dotted line) for the "small-slope" approximation. Plots are shown at different values of *Bt*. The length units of x and y are μm. (a) $m = 0.1$ (b) $m = 1$

Source: W. Zhang and J. H. Schneibel, *Comp. Mater. Sci.* **3**, 347 (1995).

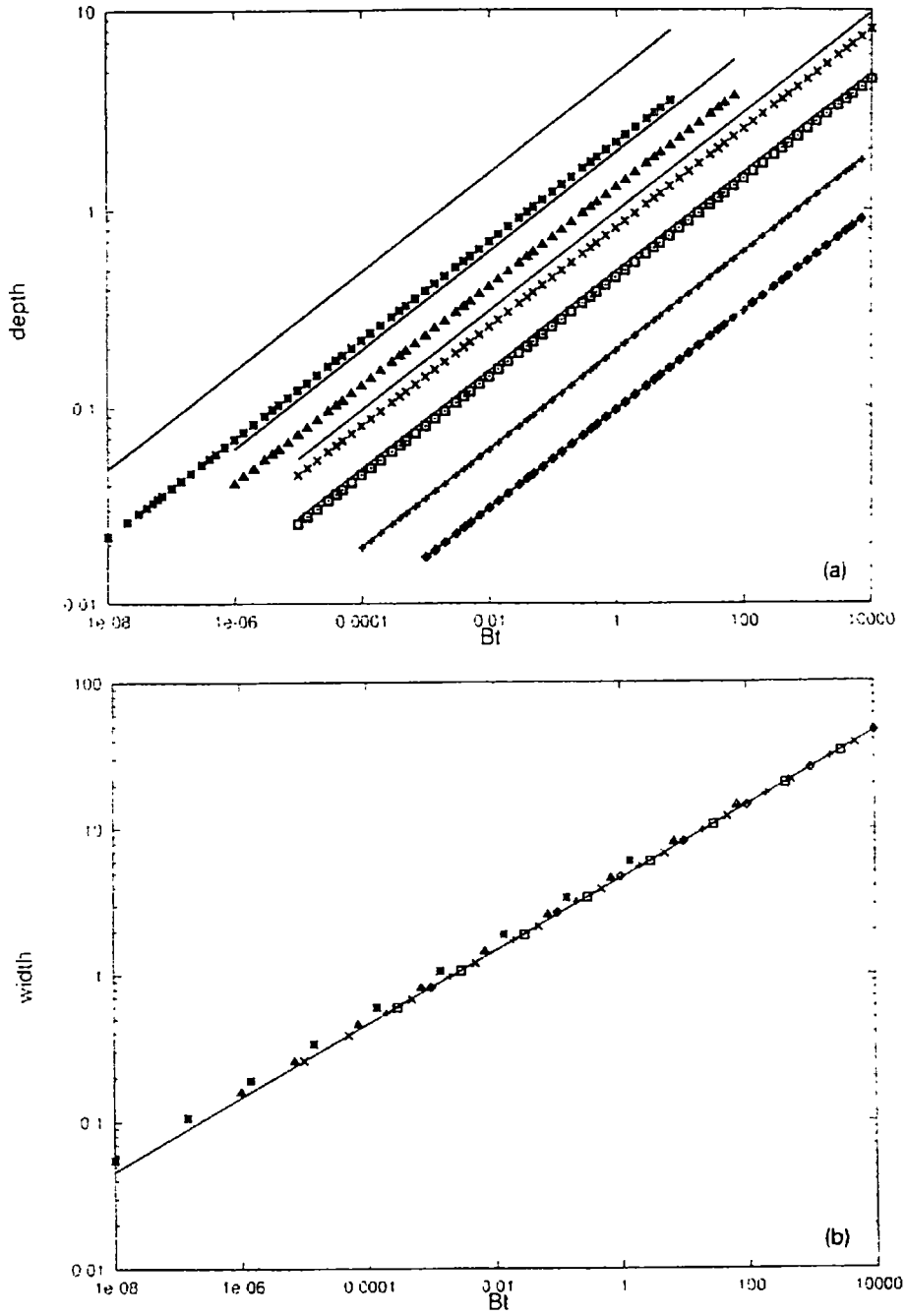

Figure 2.8. Comparison of Mullins' kinetic laws (solid lines) with the numerical solutions of Zhang and Schneibel (symbols). The units of depth and width are μm. (a) Depth as a function of *Bt* for slopes m = 0.1, 0.2, 0.5, 1, 2 and 5 from bottom to top. (b) Width as a function of *Bt* for the same slopes as in (a).

Source: W. Zhang, and J. H. Schneibel, *Comp. Mater. Sci.* **3**, 347 (1995).

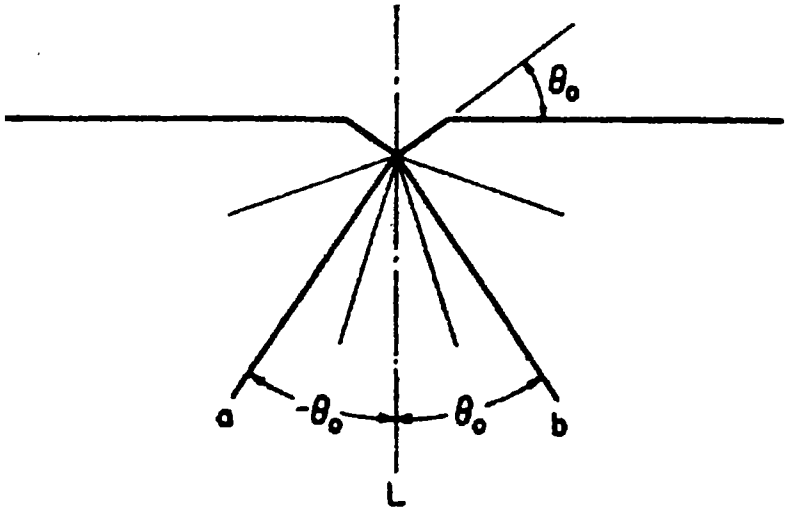

Figure 2.9 Diagram of boundary anchoring at a V-notch.

Source: W. W. Mullins, *Acta Met.* **6**, 414 (1958).

favorable. However, a grain boundary lying outside the region bounded by lines a and b can escape from the groove, shrink, and reduce its energy. Because the pinning of a grain boundary at a groove depends only on θ_o and not the groove depth, even shallow grooves can retard grain growth.[26]

2.4 Grain-Boundary Misorientation

Because grain-boundary energy ultimately determines the growth rate of a thermal groove at a fixed temperature in a specific atmosphere, the ability to control grain-boundary energy by manipulating the orientation of grains would be useful in controlling grooving in cube-textured Ni. Presumably, reducing the absolute misorientation angles between Ni grains would decrease grain-boundary energies and thus decrease grooving during the recrystallization heat treatment necessary to produce cube texture.

As discussed in Porter and Easterling,[32] the disorientation of any two bordering grains in a polycrystalline material may be described in terms of a misorientation angle ω and a single axis of rotation. By rotating one of the grains about the axis of rotation through the misorientation angle, the lattices of the grains can be aligned. In most instances, there is a complex orientation relationship between the axis of rotation and the grain-boundary plane or either lattice. However, there are two types of boundary, the pure tilt boundary and the pure twist boundary, where the axis of rotation has a simple orientation (Figure 2.10). For a tilt boundary, the axis of rotation is parallel to the boundary plane. In contrast, the axis of rotation of a twist boundary is perpendicular to the boundary plane.[32]

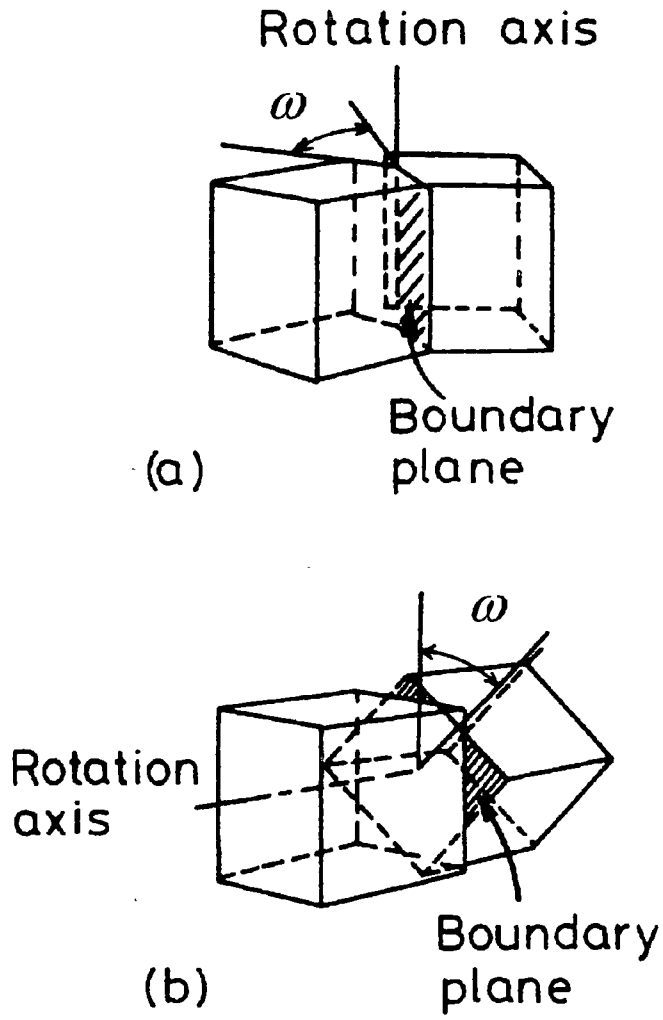

Figure 2.10. Schematic illustrations of (a) a tilt boundary and (b) a twist boundary.

Adapted from D. A. Porter and K. E. Easterling, *Phase Transformations in Metals and Alloys* 2nd ed. (Chapman and Hall, London, 1992).

In instances where the orientation of the rotation axis is complex, the misorientation of grains can be determined by using a method described by Bunge[24,33] and Bollman's theory.[4,34] In this approach, the Euler angles ϕ_1, ϕ, and ϕ_2 are used to define a rotation matrix g which describes the orientation of the crystal coordinate system $K_B(x', y', z')$ in terms of the specimen coordinate system $K_A(x, y, z)$.[4,24,33,35] The rotation matrix g is the product of the three Euler rotation matrices necessary to transform the sample coordinate system into the final orientation of the crystal coordinate system. The rotation matrix is defined as follows:[24,33]

$$g = \begin{bmatrix} \cos\phi_1 \cos\phi_2 - \sin\phi_1 \sin\phi_2 \cos\phi & \sin\phi_1 \cos\phi_2 + \cos\phi_1 \sin\phi_2 \cos\phi & \sin\phi_2 \sin\phi \\ -\cos\phi_1 \sin\phi_2 - \sin\phi_1 \cos\phi_2 \cos\phi & -\sin\phi_1 \sin\phi_2 + \cos\phi_1 \cos\phi_2 \cos\phi & \cos\phi_2 \sin\phi \\ \sin\phi_1 \sin\phi & -\cos\phi_1 \sin\phi & \cos\phi \end{bmatrix} \tag{2.9}$$

Figure 2.11 defines the Euler angles by illustrating the sequence of rotations involved in the transformation. As described by Bunge[33] and Goyal *et al.*,[35] the crystal coordinate system and the sample coordinate system are initially aligned. Next, the crystal coordinate system is rotated about the crystal z' axis through ϕ_1 in the range $0 \leq \phi_1 \leq 2\pi$. Then, it is rotated about the crystal x' axis through ϕ in the range $0 \leq \phi \leq \pi$. Finally, it is rotated about the crystal z' axis through ϕ_2 in the range $0 \leq \phi_2 \leq 2\pi$.[33,35] The absolute grain orientations obtained from this process can be used to calculate grain-boundary misorientation angles. For example, the absolute misorientation angle between two grains can be determined from the misorientation matrix $g12 = g1^{-1}g2$ where $g1$ and $g2$ are the absolute orientations of grains 1 and 2, respectively.[4,34,35]

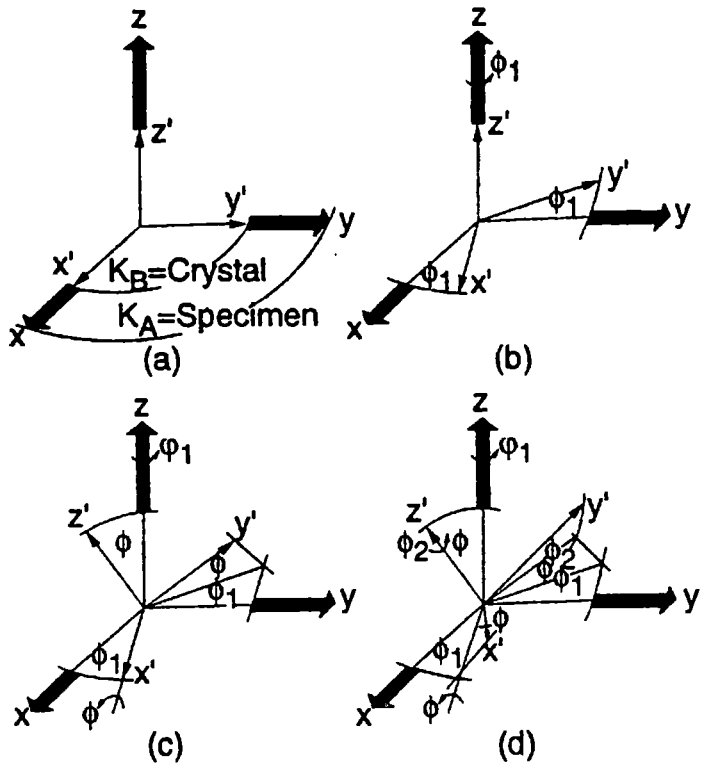

Figure 2.11 Illustrations of the Euler angle rotations which describe the final orientation of a crystal coordinate system K_B with respect to the sample coordinate system K_A. (a) K_B is aligned with K_A, (b) rotation ϕ_1 about z', (c) rotation ϕ about x', and (d) rotation ϕ_2 about z'.

Source: A. Goyal, E. D. Specht, D. M. Kroeger and T. A. Mason, *Appl. Phys. Lett.* **68**, 711 (1996).

CHAPTER 3

EXPERIMENTAL PROCEDURE

3.1 Material

For this research, a length of RABiTS tape previously prepared by Dr. Amit Goyal and Ed Hatfield of Oak Ridge National Laboratory was obtained in the as-rolled condition. The tape was rolled from a randomly oriented, polycrystalline rod of 99.99% pure Ni and had a final thickness of 125 μm. A highly polished surface was achieved from the rolling process. For record keeping purposes, this material was designated S-30.

3.2 Sample Preparation

For examination with the atomic force microscope, small samples were cut from a large piece of S-30 tape. In the first step of the preparation process, an "X" was scratched in a corner of one side of the large piece of tape. Then, a permanent marker and a straight edge were used to draw lines across the width of the tape every 3 mm, marking the pieces to be cut off. An "X" was also scratched near each edge of the sample pieces to be removed on the same side that the large tape was marked with an "X". This was done so that an identical side of each sample ("X" or no "X") could identified and examined at any time during the experiment. Thus, any variations in the microstructure between the two polished surfaces of the tape could not affect the experimental results. Next, a table-top

shear was used to remove the samples from the large tape by making cuts perpendicular to the rolling direction of the tape, and the rough edges of the sample pieces were trimmed off. Lastly, the 3mm wide sample pieces were cut parallel to the rolling direction to form halves, each with a length of approximately 12 mm.

After sectioning the tape, the samples were cleaned by dipping them into acetone and then pure ethanol. To minimize spotting, a heat gun was carefully used to evaporate the ethanol.

A Lindberg model 55332, ultra-high vacuum, tube furnace was used to anneal the as-rolled Ni and thereby obtain the desired cube texture. With the "X"-sides facing upward, the samples were placed in an annealing boat made of tantalum metal (a very strong oxygen getter) to reduce the possibility of oxidation during annealing. Also, before annealing, the furnace was closed and preheated to remove water vapor. Samples were annealed for 10, 30, 60, and 120 minutes at 600 and 800°C and for 10 and 30 minutes at 1000°C. Temperature profiles were recorded using a platinum-10% rhodium vs. platinum (type-s) thermocouple and a Gould model 15-4628-10 chart recorder. An appropriate 120 μV room temperature correction was applied to the recorder data. To prevent oxidation, the samples were allowed to cool slowly under vacuum in the furnace after the power was turned off. A typical annealing cycle is plotted in Figure 3.1. The flat portion of the graph represents the annealing time.

Using silver paint as an adhesive, each sample was mounted on a 25 mm diameter, Hitachi SEM sample stub after the annealing process. The samples were then placed one at a time in a Nano II nanoindenter, and a square array of 121 indentions was

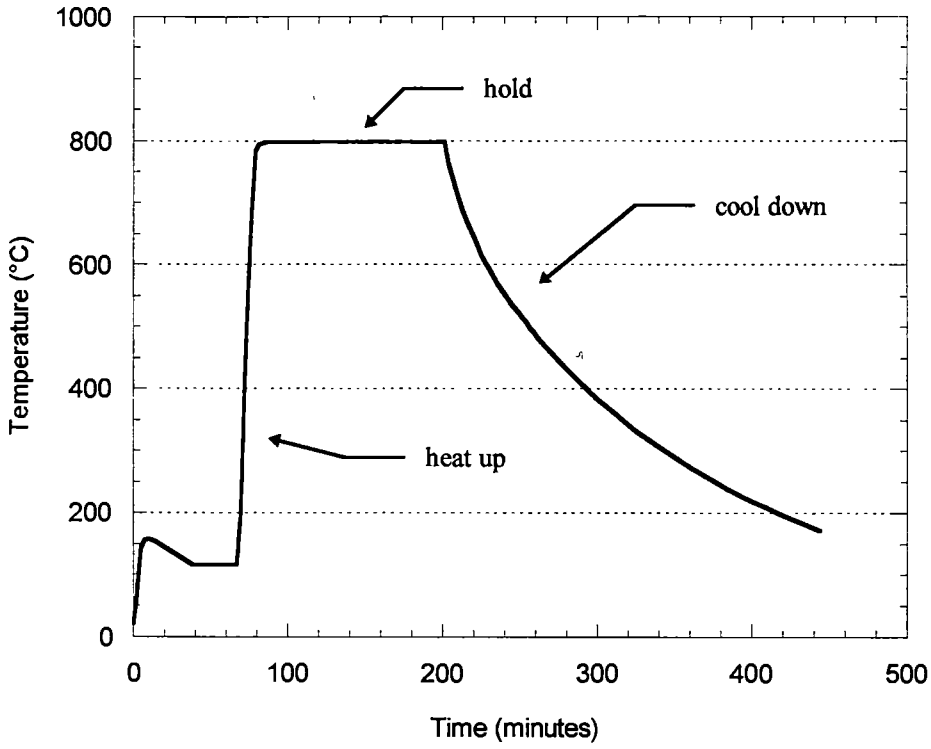

Figure 3.1 Typical recrystallization annealing cycle for RABiTS Ni. The hold time at 800°C was 2hrs.

automatically made in the center of the surface of each specimen. The indentations were spaced every 200 μm in the x and y-directions and formed a 100 element array of squares which was used to position the tip of the AFM and to catalog the position of triple points examined with the AFM. The shape of the indented array is shown in Figure 3.2, and actual indentations in the surface of a sample are shown in Figure 3.3. Finally, after the indentation routine was completed, the arrays were examined for completeness, and the samples were removed from the nanoindenter.

3.3 AFM Measurements

After being removed from the nanoindenter, the samples were examined using a Park Scientific, Auto Probe XL, atomic force microscope. For reliability, the instrument was operated in contact mode. Also, prior to collecting any scan images, the 100 μm AFM scanner was calibrated. This was done by obtaining dimensional standards for calibrating the measurements made by the AFM in the *x* (width), *y* (length), and *z* (height) directions and using them to adjust the response of the scanner. Scanning parameters (Table 3.1.) were adjusted and optimized by scanning standards and samples.

A 9.9 μm grid calibration grating and a 1.0 μm periodic grating were used to calibrate the x and y response in high power mode. The calibration procedure outlined in the Auto Probe user's guide[36] was followed precisely. After the calibration, the error in these measurements due to the scanner response was found to be only 0.6%. To calibrate the z response, four different step height standards were used. The specifications for these standards are listed in Table 3.2. A Tencor, Alpha-Step 500 profilometer was used to

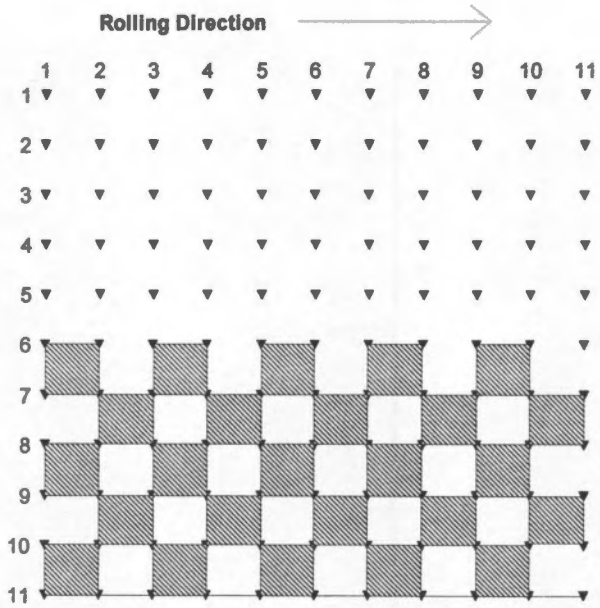

Figure 3.2. Diagram of the nanoindentation grid used to locate grain-boundary triple points. The gray squares indicate elements which were examined.

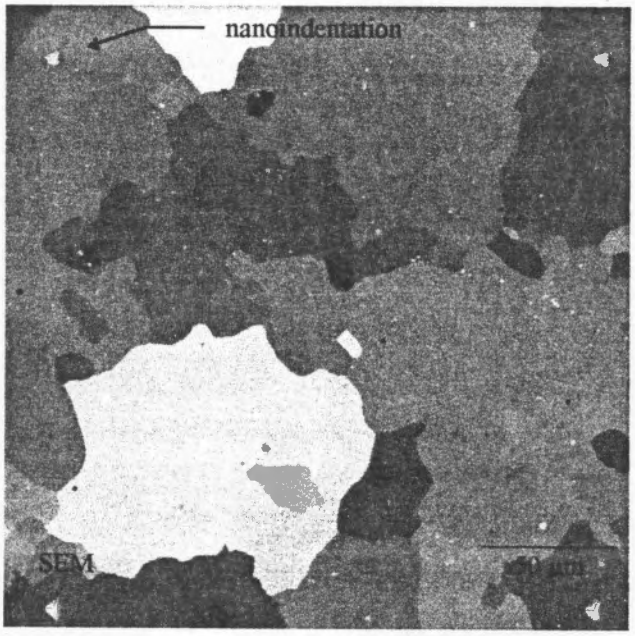

Figure 3.3. SEM micrograph of four nanoindentations in RABiTS Ni, forming one element of the array shown in Figure 3.2.

Table 3.1. Optimal scanning parameters for imaging triple points in RABiTS Ni with the Park Scientific AutoProbe XL atomic force microscope.

Probe Type	Contact
Imaging Mode	Topogaphic
Fast Scan Direction	X
X Scan	Right to left
No. of Columns	256
No. of Rows	256
X Scan Size (μm)	10.6
Y Scan Size (μm)	10.6
X Scan Rate (Hz)	0.25
Z Frequency Response (Hz)	800
Z Gain	7.00
Tip Force (nN)	-300 to -100

Table 3.2 Specifications for AFM calibration standards.

Standard Type	Manufacturer	Step Size (Å)	Tolerance (Å)
Step - CeO_2/Ni	ORNL	1000	N/A
Square Pits - SiO_2	Digital Instruments	1936	±63
Step - Si/SiO_2	Tencor Instruments	8140	N/A
Step - Si/SiO_2	Tencor Instruments	9120	N/A

confirm the step height of the 1000, 8140, and 9120 Å standards. The *x-y* linear resolution of the profilometer was not sufficient to confirm the depth of the pits in the 193.6 nm VLSI standard.

The *z*-piezo response of the AFM was found to be nonlinear, and the measurement error in the *z* direction increased with increasing step height. This behavior is shown in Figure 3.4 with a 2nd-order polynomial fit to the response data. Due to this effect and because measurements were to be made on grain-boundary grooves expected to range from 100 to 2000 Å in depth, the *z*-piezo response was calibrated to the 193.6 nm ± 6.3 nm VLSI standard so that the measurements could be made with little or no correction. Also, the step height of this standard was known with the greatest accuracy. As a final calibration step, a noise test was run on the AFM which revealed that there was electrical noise in the feedback system with an amplitude of approximately 5 Å rms. Lastly, the manufacturer-reported control resolution[37] of the AFM electronics and mechanics in the *z* direction is the *z* range on the image divided by 2^{16}. For the measurements made in this study, this is a very small fraction of an Angstrom (≈0.005 - 0.010 Å) and is not the limiting factor for the overall resolution of the AFM.

Following the calibration, the AFM was used in topographic (constant force) mode to image randomly selected, thermally grooved, grain-boundary triple points. By scanning triple points, three grain boundary grooves were imaged in every scan. To minimize the effects of thermal drift, samples were placed in the AFM at least two hours prior to scanning. Also, to minimize the visual impact of rolling lines in the scans, the fast scan direction was oriented parallel to the rolling direction of the samples. Orienting the fast

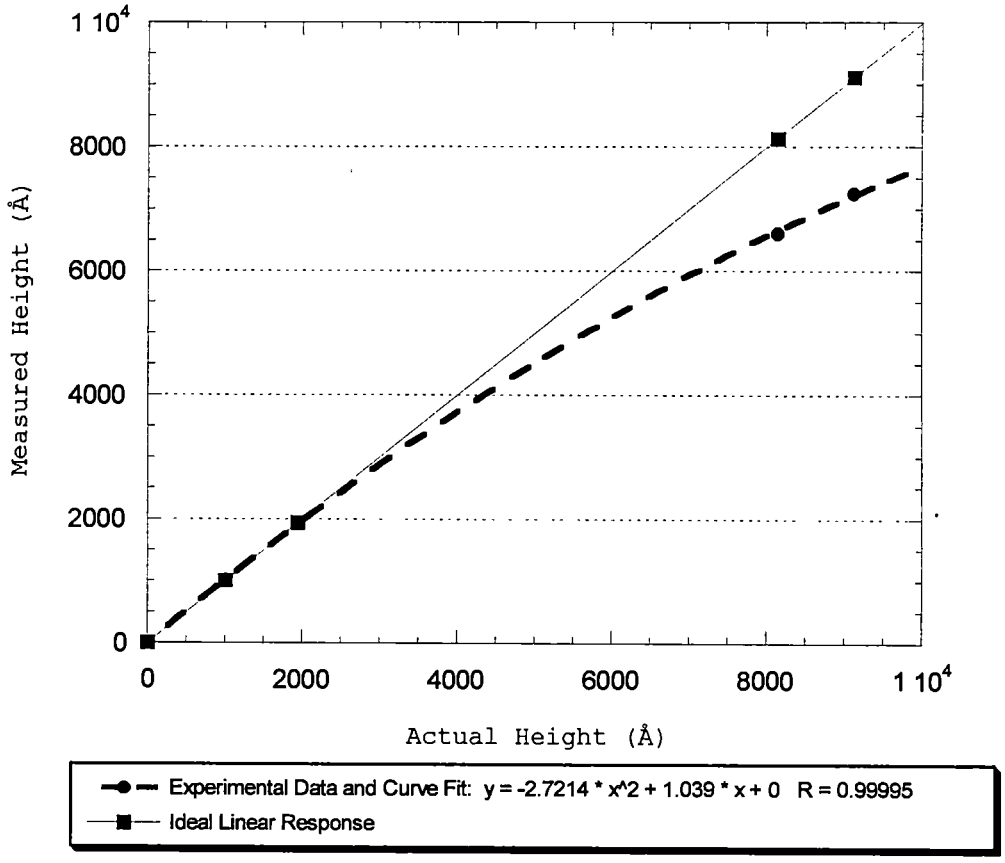

Figure 3.4. Calibration plot for the Park Scientific AutoProbe XL showing the deviation of the *z*-piezo response from linearity.

scan direction perpendicular to rolling lines would cause the tip to "jump" or "bounce" over such raised features.

Starting at the bottom, left element of the nanoindented array (see Figure 3.2), one grain-boundary triple point in every other square for half of the array on each specimen was imaged in a 10.6 x 10.6 μm, 256 x 256 pixel, line scan, producing twenty-five scans per sample. First, using the optical microscope attached to the AFM, a triple point was selected within the element of interest. Then, the tip was lowered and made to scan a single line continuously (right to left) in order to adjust the scanning force. Typically, this force was -100 to -300 nN and was extremely dependent on the sample. So that the specific triple points which had been scanned could be found on the samples at a later time, sketches were made of the grain-boundary networks within the array elements, and the triple points were marked. The images from each sample were stored in a computer database for later analysis.

Before any measurements of grain-boundary groove dimensions were made, it was necessary to digitally process the AFM images previously collected. The processing involved using the PSI Proscan Image Processing (ver. 1.10) computer program to apply a 0th-order flattening routine which removed slope from the images without distorting the critical data. The removal of slope from the images was essential in order to make accurate, reliable measurements of grain-boundary depth, width, and equilibrium angle.

The Proscan Image Processing computer program was also used to perform measurements of grain-boundary groove dimensions. "Electronic" cross sectional lines were drawn across the grain boundaries in a two-dimensional scanned image which was

displayed on a computer monitor, and point markers were used to make individual measurements of depth, width, and equilibrium angle along the corresponding profile of the surface topography. Figure 3.5 (a, b, c, and d) depicts how a cross sectional line was drawn and how the measurements were made. Five sets of measurements were made along the length of each grain-boundary groove joining at a triple point. The data were recorded and later analyzed and plotted.

3.4 EBSD Analysis

Electron back-scattered diffraction (EBSD) was used to determine the absolute misorientation angle between each of the Ni grains imaged in the AFM scans. Data were collected using a Philips XL-30 Field-Emission SEM equipped with a silicon intensified target camera (SIT). Each sample was placed in the SEM and tilted toward the camera at 70° to the incident electron beam. The triple points which had been previously imaged with the AFM were located by navigating the nanoindented array and referring to the sketches of the grain-boundary networks. Once a particular triple point was found, the diffraction patterns of the adjoining grains were collected and indexed using orientation image microscopy (OIM) software. Also, a micrograph of the triple point was made and stored. The absolute orientation of each grain was determined from the indexed diffraction patterns and stored in a computer database. Bollman's theory[4,34] was used to determine the grain-boundary misorientation between two bordering grains. Crystallographically, there may be many symmetrically equivalent forms of the angle/axis

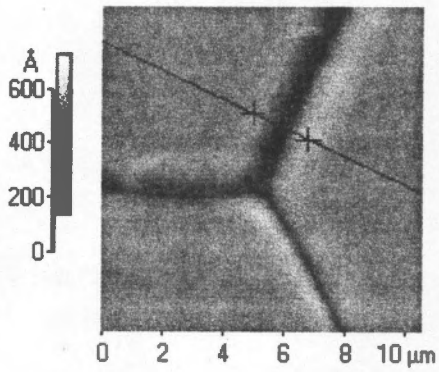

(a) Measurement line drawn on 2-D image

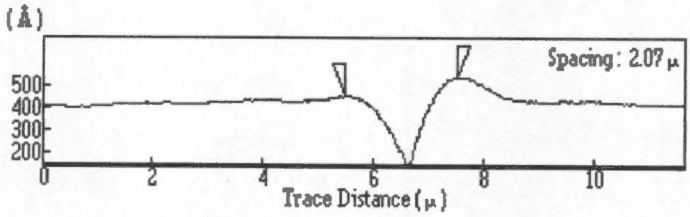

(b) Width measurement on line trace of groove

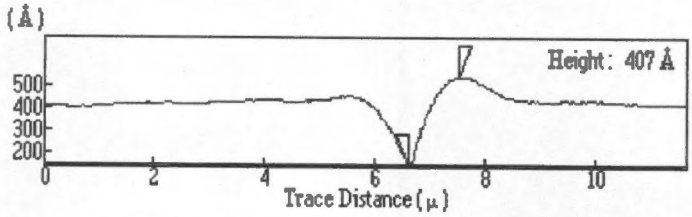

(c) Height measurement on line trace of groove

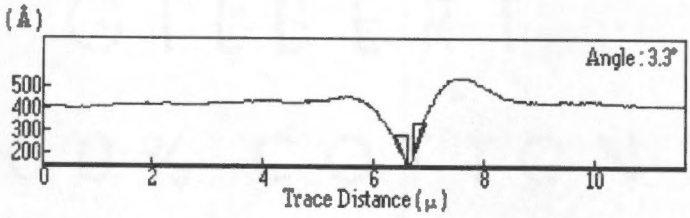

(d) Equilibrium angle measurement on line trace of groove

Figure 3.5 Illustrations showing various measurements which were made from AFM images of triple points

of misorientation. Thus, the disorientation is characterized by the form with "the smallest positive misorientation angle."[4,35]

3.5 X-ray Diffraction Analysis

X-ray diffraction pole figures were generated to characterize the cube texture of samples which had been examined using atomic force microscopy and electron back-scatter diffraction. A Picker, 4-circle, x-ray diffractometer with a $Cu_{K\alpha}$ source and a graphite diffracted beam monochromator was used to generate a pole figure from the 800°C, 10 min. specimen. The Picker was operated at 40 kV and 10 mA. Because the Picker later failed, a Huber diffractometer with a $Cu_{K\alpha}$ rotating anode source and a graphite incident beam monochromator was used to obtain pole figures from the 800°C, 30, 60 and 120 min. samples. This machine was operated at 50 kV and 40 mA. The pole figures from the two machines are comparable.

Before being placed in a diffractometer, a sample was carefully removed from its SEM sample stub and magnetically mounted on a sample oscillator. The position of the sample on the oscillator was adjusted so that the x-ray beam would impinge only on the sample. Next, the sample was placed in the goniometer, and the diffractometer x-ray source was energized. The pole figure routine was initiated on the data acquisition computer, and a pole figure was collected. Finally, the data were archived. This procedure was repeated for each sample.

3.6 Grain Size Measurements

ASTM Specification E 112-96 was used as the guideline for making measurements of grain size. First, the samples were etched using glyceregia, consisting of 15 ml HCl, 5 ml HNO_3, and 15 ml glycerin.[38] The etchant was applied with a cotton swab for 90 seconds and then washed off with water. The samples were then cleaned with ethanol and dried with a heat gun. Next, a Nikon Microphot-SA, light microscope was used to make bright-field photomicrographs of the surface of each sample. For each sample, five blindly selected fields were photographed at 100 X using Polaroid Type 55 film. The Abrams three-circle method for determining grain size was applied to these five different fields and grain-boundary intersections were counted. Then, the mean lineal intercept, its mean value, its standard deviation, 95% confidence limit, and percent relative accuracy were calculated. Finally, the grain size was calculated.

CHAPTER 4

RESULTS AND DISCUSSION

4.1 Qualitative Observations of Thermal Grooving in Cube-Textured Ni

In this study, some important qualitative observations were made concerning thermal grain-boundary grooving on thin strips of cube-textured nickel. In this section, thermal groove morphologies, the continuity of groove networks, and an annealing phenomenon are discussed.

Diffusion-induced thermal grooves were observed in AFM scans of several nickel specimens. Such grooves are formed during high temperature annealing by the surface diffusion of atoms away from the intersection of the grain boundary with the surface. Figure 4.1 (a and b) shows two views of an AFM scan of diffusion-induced grooves at a triple point. Clearly, these grooves exhibit the characteristic, diffusion-induced, convex ridges adjacent to the grain boundary-surface intersections. Diffusion-induced grooves were found on samples that had been annealed at 600 and 800°C. However, in the 600° C samples, no diffusion-induced grooves were observed at 10 minutes of annealing, and only faint grooves were found sporadically distributed on the surfaces of specimens annealed for 30, 60, and 120 minutes. In the 800°C samples, complete networks of well defined diffusion-induced grooves were found at all annealing times (Figure 4.2).

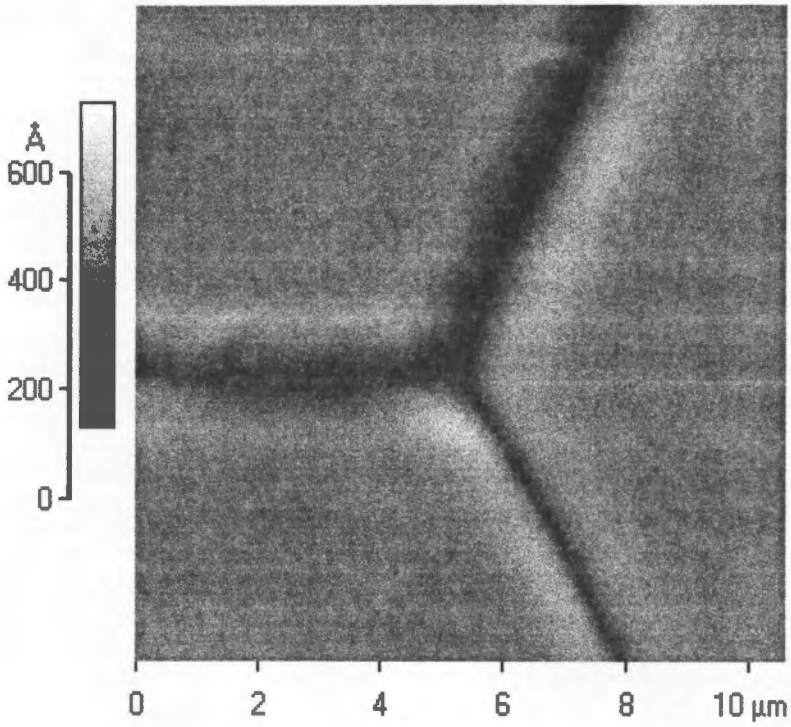

(a)

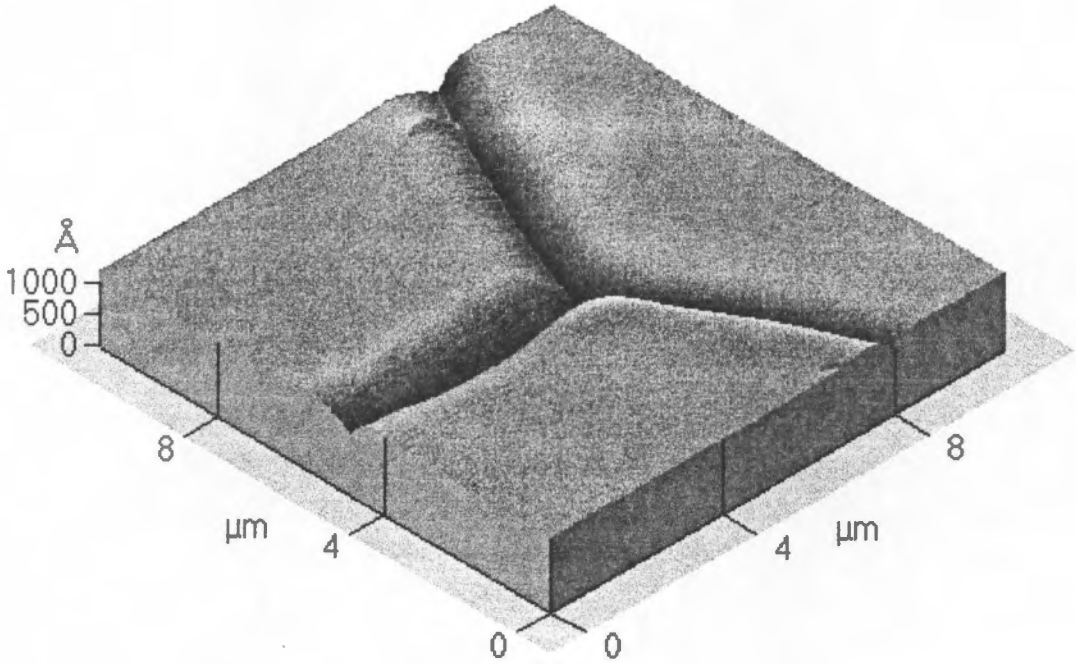

(b)

Figure 4.1. AFM scan of diffusion-induced thermal grooves at a triple point in cube-textured Ni. Annealed at 800°C, 2hrs. (a) 2-D view and (b) 3-D view (vertical exaggeration ~ 10X).

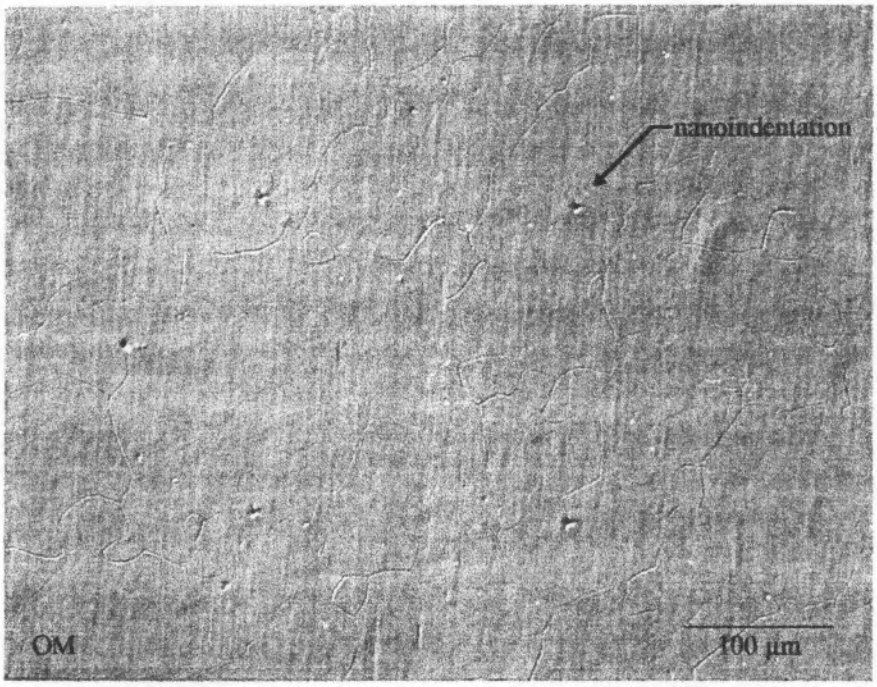

Figure 4.2. Photomicrograph of diffusion-induced, thermal grain-boundary grooves on the surface of cube-textured Ni. Annealed at 800°C, 2hrs. The degree of grooving is similar at lower annealing times.

On some samples, thermal grooves were observed to be highly faceted and did not exhibit the characteristics of diffusion-induced grooves. These faceted grooves were found on samples annealed at 800°C for 30, 60, and 120 minutes and on samples annealed for 10 and 30 minutes at 1000°C. Two views of an AFM scan of faceted grooves are shown in Figure 4.3 (a and b). It is notable that the interior surfaces of the adjacent grains are also faceted. The grooves and interior facets are thought to be formed by the evaporation of surface atoms to a vacuum environment during high temperature annealing. At annealing temperatures of 800 and 1000°C, faceted grooves formed well defined, complete networks. Interestingly, faceting and diffusion-induced grooving were not found to occur together.

An examination of samples with the AFM immediately after the annealing process revealed a very interesting and important annealing phenomenon. For samples annealed at a temperature of 800°C, diffusion-induced grooves were observed to always form on the side of a sample that faced the annealing boat, and faceting always occurred on the side that faced away from the boat. Thus, it may be hypothesized that the local atmospheres in contact with either side of a sample during annealing differed substantially. As a result, the mode of groove formation on each side of a particular sample also differed.

In the case of a sample surface facing the annealing boat, evaporated Ni atoms became trapped between the sample and the boat. Because of this effect, the metal surface quickly reached quasi-equilibrium with its vapor, and further evaporation of atoms from the surface was minimal. Thus, groove formation was controlled by surface diffusion, and diffusion-induced grooves formed on the boat-side of the sample.

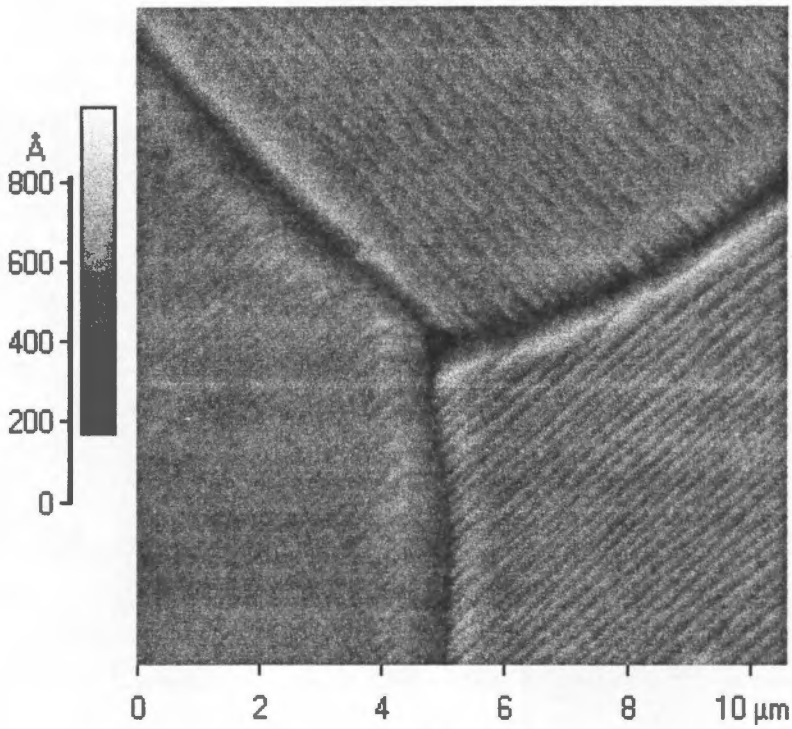

(a)

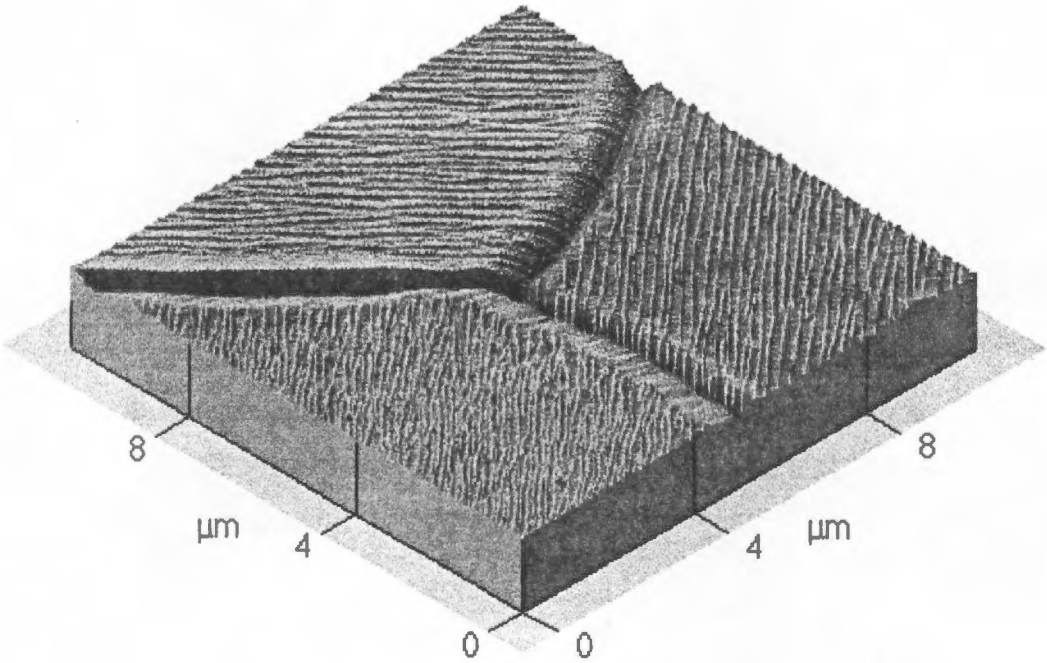

(b)

Figure 4.3. AFM scan of faceted thermal grooves at a triple point in cube-textured Ni. Annealed at 800°C, 2hrs. (a) 2-D view and (b) 3-D view (vertical exaggeration ~ 10X).

In contrast, for a sample surface facing away from the boat and toward vacuum, the metal surface was never able to reach equilibrium with its vapor, and Ni atoms evaporated continuously. The evaporation of surface atoms led to the formation of faceted thermal grooves and grain surfaces.

A faceted Ni surface would be unsuitable for the subsequent deposition of buffer layers because of the large quantity of sharp ridges present. The ridges, which are frequently observed to be 100 Å high, would likely act as surface defects and contribute to the cracking and/or delamination of layers deposited on the cube-textured Ni. In contrast, the smooth Ni surface formed by the surface diffusion of atoms would probably be a superior substrate for the epitaxial growth of oxide layers. In this case, diffusion-induced grain-boundary grooves would be the only defects. Thus, only diffusion-induced grooves warrant further analysis in this study.

In addition, it should be noted that faceting precludes the possibility of making reliable measurements of groove width, depth, and equilibrium angle. For a faceted groove, convex surface maxima do not exist, and thus depth and width can not truly be defined. Also, the equilibrium angle is likely to change suddenly along the length of a faceted groove, preventing it from being accurately measured.

Because diffusion-induced grooves were not very prominent on samples which were annealed at 600°C, and only faceted grooves formed at 1000°C, measurements of groove dimensions were only made on the 800°C samples. Diffusion-induced grooves were large enough on the 800°C samples to be located with the optical microscopes on the nanoindenter and the AFM. Concerning the 600°C samples, grooves could not be

seen easily with the AFM optical microscope, making the positioning of the AFM tip for measurements very difficult or impossible.

4.2 Effect of Annealing Time on Thermal Groove Dimensions

For the samples annealed at 800°C, the discrete measurements of groove depth and width made with the AFM were used to calculate the average depth and width of each thermal groove that was analyzed. This was done to obtain the best estimate of the true depth or width for each groove. These averages were used to generate distribution plots of depth and width for annealing times of 10, 30, 60 and 120 minutes. The histograms in Figure 4.4 (a, b, c, and d) and Figure 4.5 (a, b, c, and d) illustrate the changes in the distribution of grain-boundary groove widths and depths, respectively, with increasing annealing time. Gaussian curves were fitted to each of the histograms, and the correlation coefficient R for each fit indicates good agreement with the data. Furthermore, this indicates that the distributions are essentially normal. Also, from these histograms, it can be seen that the width and depth distributions broaden with time and that the mean of these distributions increases with time. For the 10, 30, 60 and 120 minute histograms of Figure 4.4, the mean values of groove width are 1.25, 1.46, 1.78, and 1.68 μm, respectively. Also, for the 10, 30, 60, and 120 minute histograms in Figure 4.5, the mean depths are 180, 237, 241, and 292 Å, respectively. The maximum depth measured in the experiment was about 650 Å; however, grooves with depths exceeding 1500 Å were occasionally found during casual microscopic observations. These deep grooves usually occurred around grains with a diameter of 10-20 μm.

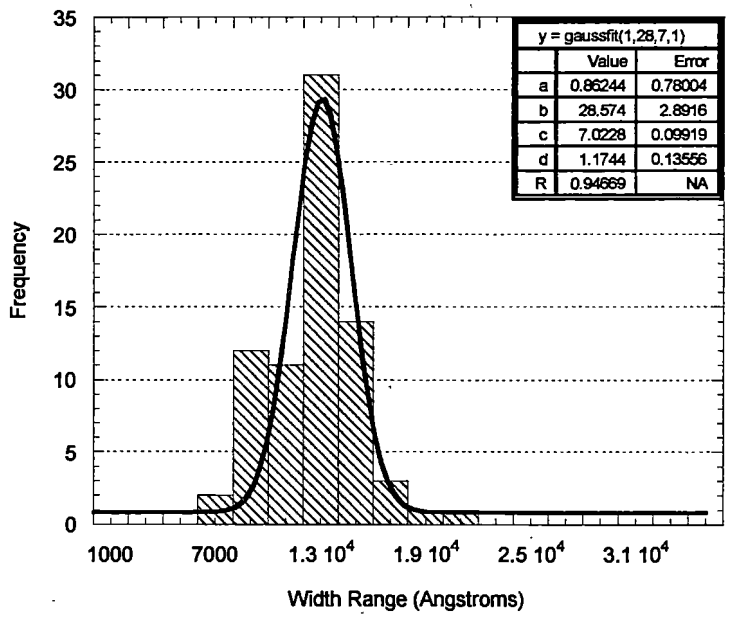

(a) Annealed at 800°C, 10 min.

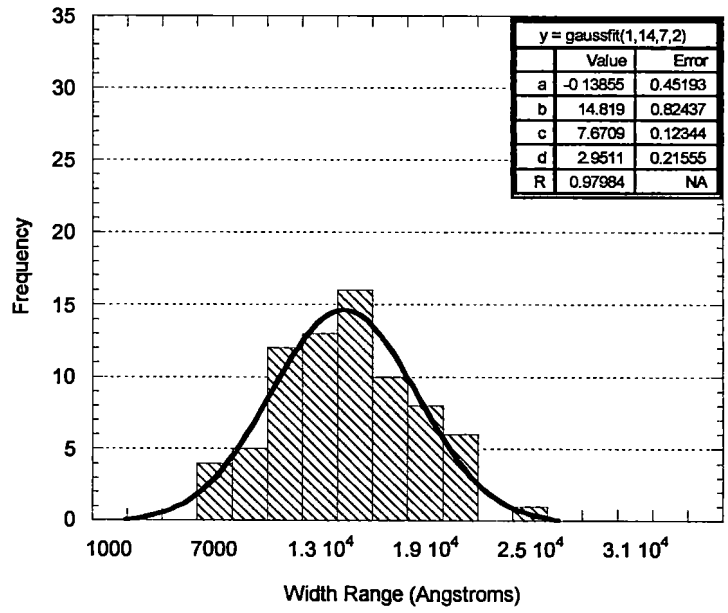

(b) Annealed at 800°C, 30 min.

Figure 4.4. Distributions of grain-boundary groove, average widths in cube-textured nickel.

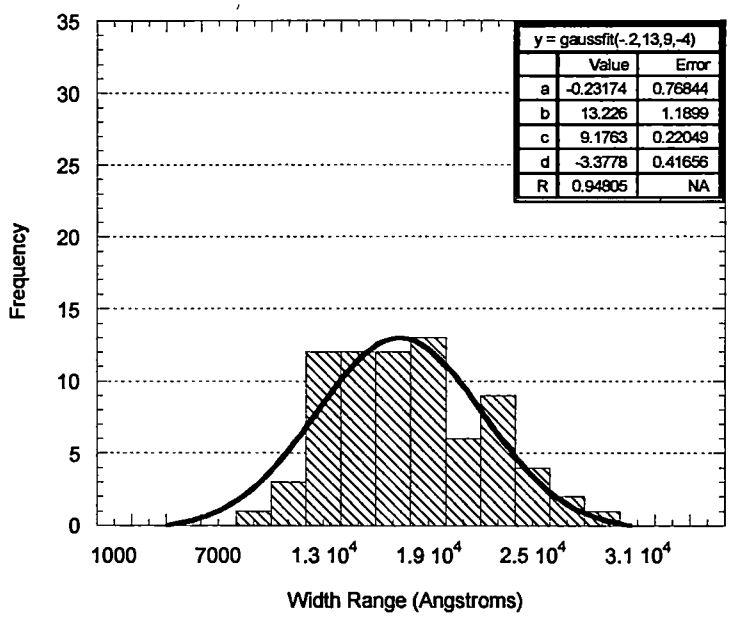

(c) Annealed at 800°C, 1 hr.

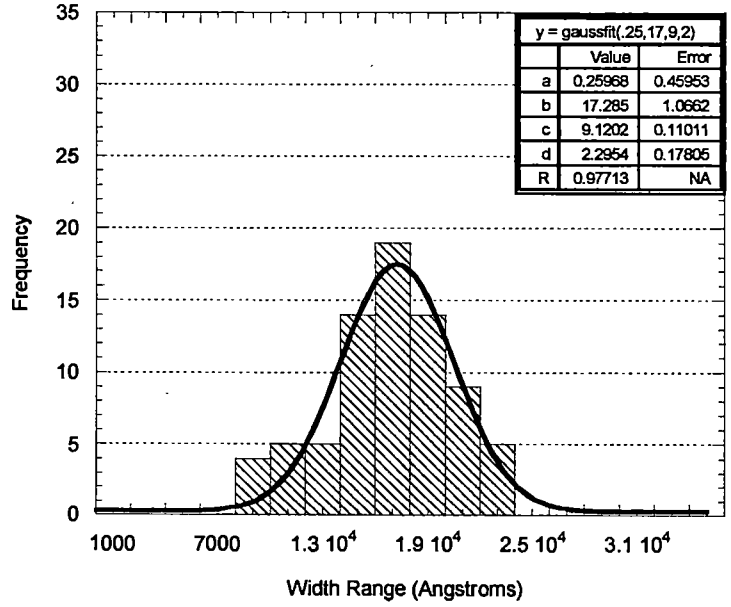

(d) Annealed at 800°C, 2hrs.

Figure 4.4. (continued)

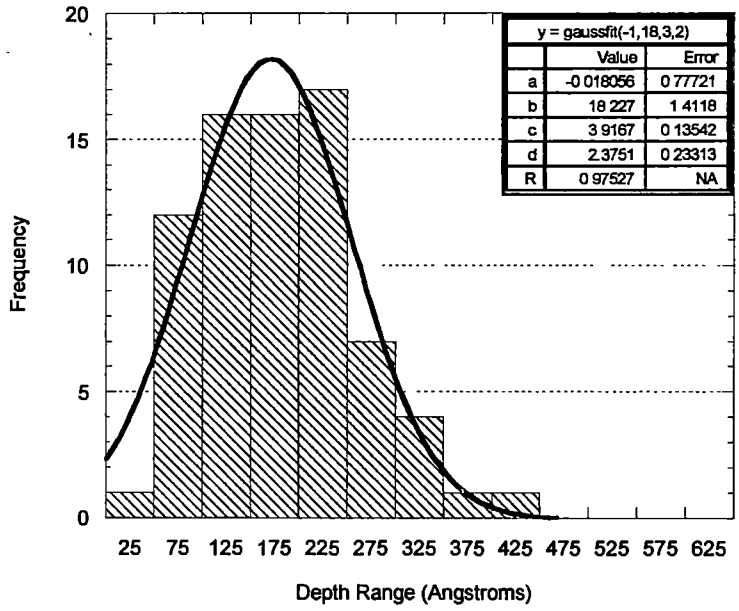

(a) Annealed at 800°C, 10 min.

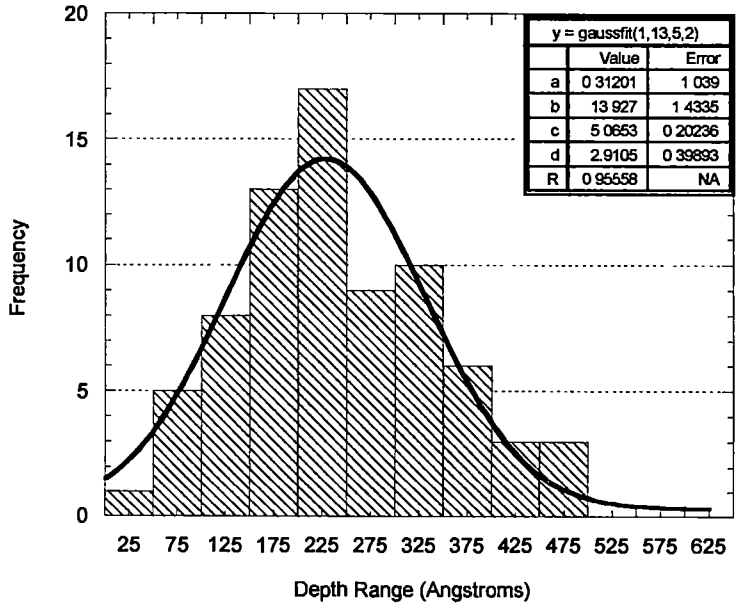

(b) Annealed at 800°C, 30 min.

Figure 4.5. Distributions of grain-boundary groove, average depths in cube-textured nickel.

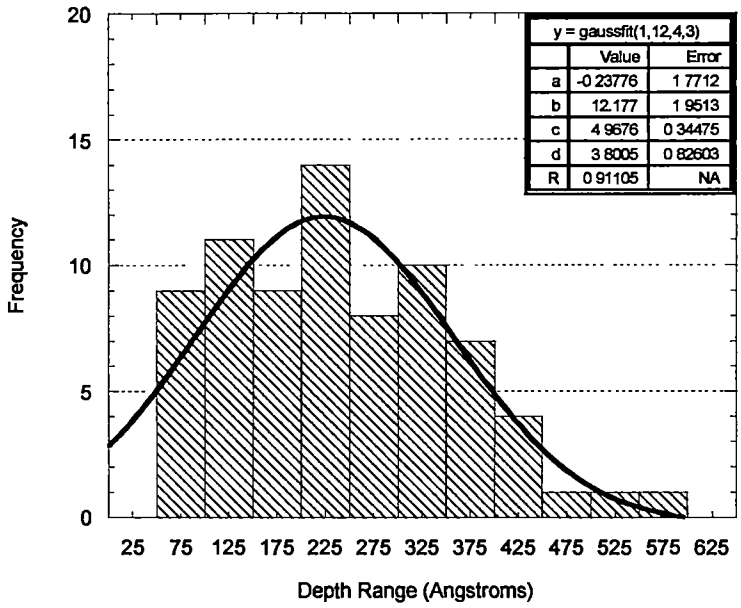

(c) Annealed at 800°C, 1 hr.

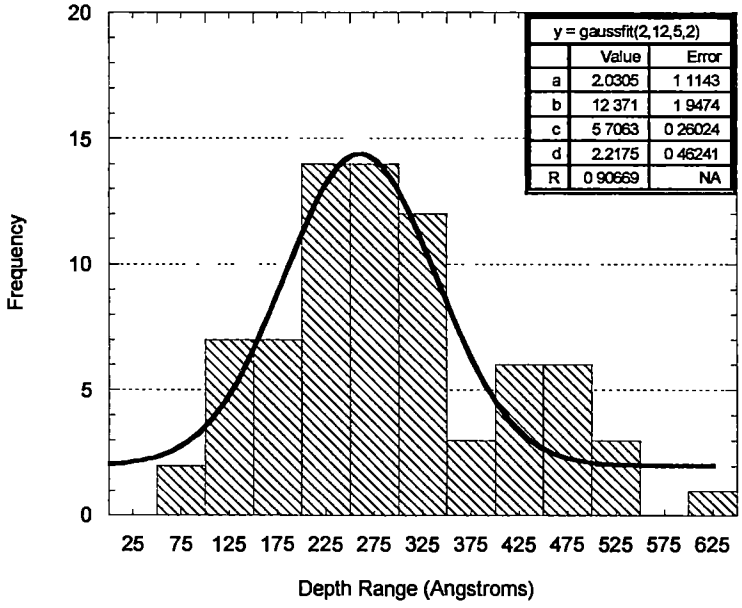

(d) Annealed at 800°C, 2 hrs.

Figure 4.5. (continued)

A close examination of the mean, groove width and depth data reveals that the magnitudes of these dimensions increase with time in accordance with Mullins' theory[25] of groove growth by surface diffusion. In Figure 4.6, the mean widths are plotted against time, and a curve is fitted to the data using an equation with the general form of Equation 2.6 as follows:

$$y = a*(x)^{\frac{1}{4}} \tag{4.1}$$

where

y = groove width (cm)
x = the independent variable, time (s)
a = the coefficient , $4.6B^{\frac{1}{4}}$ (cm/s$^{1/4}$)

As can be seen, the curve fit is in good agreement with the data. Using Equation 4.1 to fit a curve to the mean groove depths also produces good results (Figure 4.7). In this case

y = groove depth (cm)
x = the independent variable, time (s)
a = the coefficient, $0.973mB^{\frac{1}{4}}$ (cm/s$^{1/4}$)

Also, to show that the deepening of grooves in this experiment was driven by surface diffusion and not evaporation-condensation, the data in Figure 4.7 is fitted with an equation of the general form of Equation 2.7:

$$y = b*(x)^{\frac{1}{2}} \tag{4.2}$$

where

y = groove depth (cm)
x = the independent variable, time (s)
b = the coefficient, $1.13mA^{\frac{1}{2}}$ (cm/s$^{1/2}$)

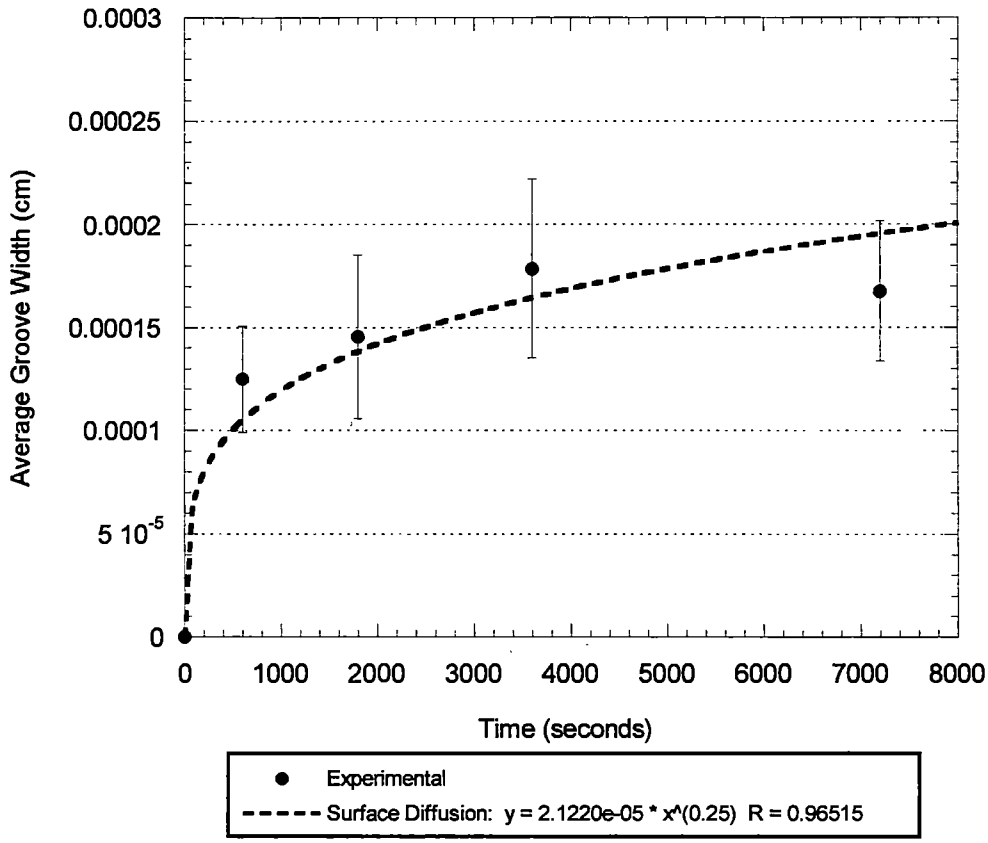

Figure 4.6 Average width of thermal grooves as a function of time for cube-textured nickel annealed at 800°C. The dashed line is a curve fit to the data. Error bars indicate standard deviation about the mean.

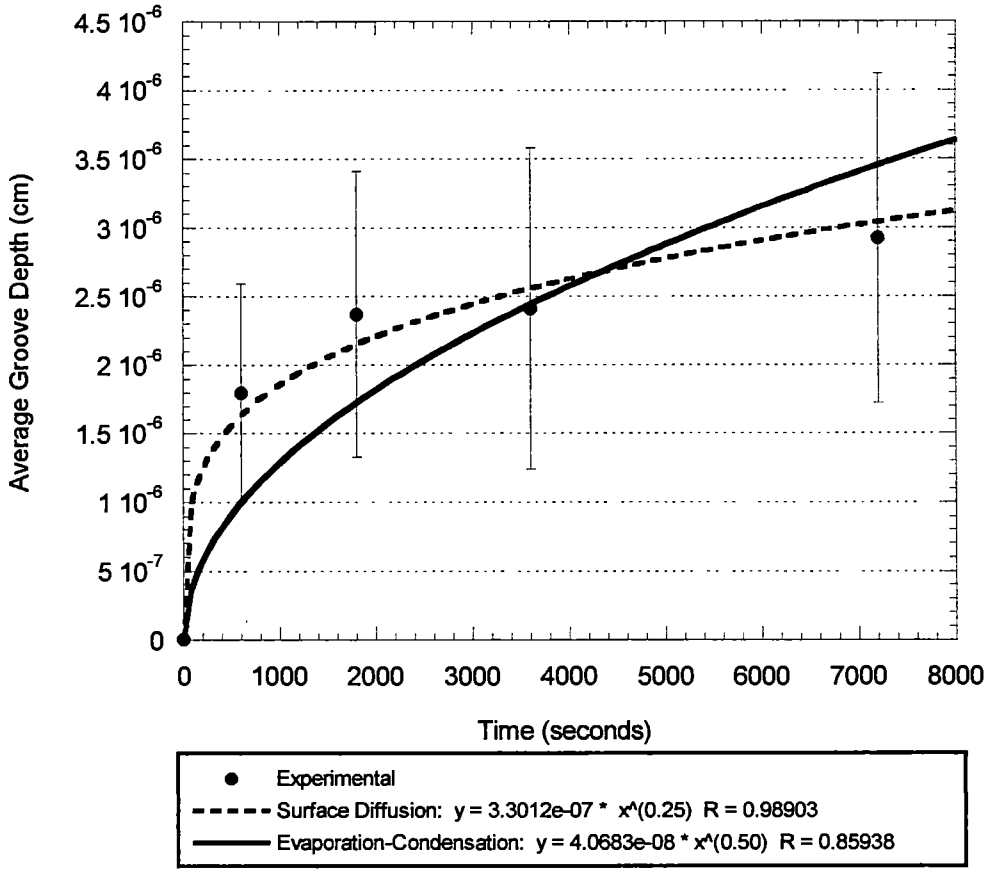

Figure 4.7. Average depth of thermal grooves as a function of time for cube-textured nickel annealed at 800°C. Curve fits are shown for surface diffusion and condensation-evaporation. Error bars indicate standard deviation about the mean.

It is readily apparent that the curve fit calculated with Equation 4.2 does not agree with the data as well as the curve fit given by Equation 4.1. This strongly indicates that the deepening of grooves is diffusion-induced.

From the data presented in Figures 4.6 and 4.7, it can be seen that the growth of a groove is initially very rapid. In fact, considering the curve fit in Figure 4.7 for the surface-diffusion growth of grooves, the average depth of a groove after 30 minutes of annealing is 71% of its depth after 2 hours of annealing. Thus, one method of minimizing thermal grooving in RABiTS Ni would be to use the absolute shortest annealing time which produces a sharp cube texture.

4.3 Effect of Equilibrium Angle on Groove Depth

Another factor which profoundly affects the deepening of a thermal groove is the magnitude of the equilibrium angle α of the groove. The equilibrium angle is related to the slope m of the surface at the groove root (see Equation 2.4), and from Equation 2.3, it can be seen that an increase in the value of m will result in an increase in the groove depth if the variables B and t remain the same.

The plotted data in Figure 4.8 (a, b, c, and d) show the relationship between average groove depth and equilibrium angle for the samples annealed at 800°C. A linear curve fit is applied to the data in each of the graphs and forced through the origin. Generally, groove depth increases with increasing equilibrium angle for each annealing time. Also, with the exception of the graph in Figure 4.8 (d), the curve fit to the data tends to rotate about the origin in a counterclockwise direction as time increases. Because

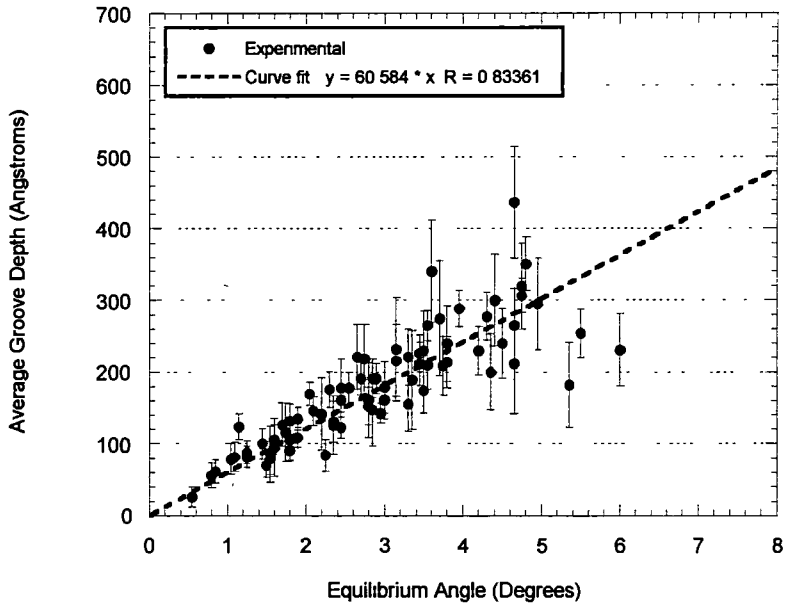

(a) Annealed at 800°C, 10 min.

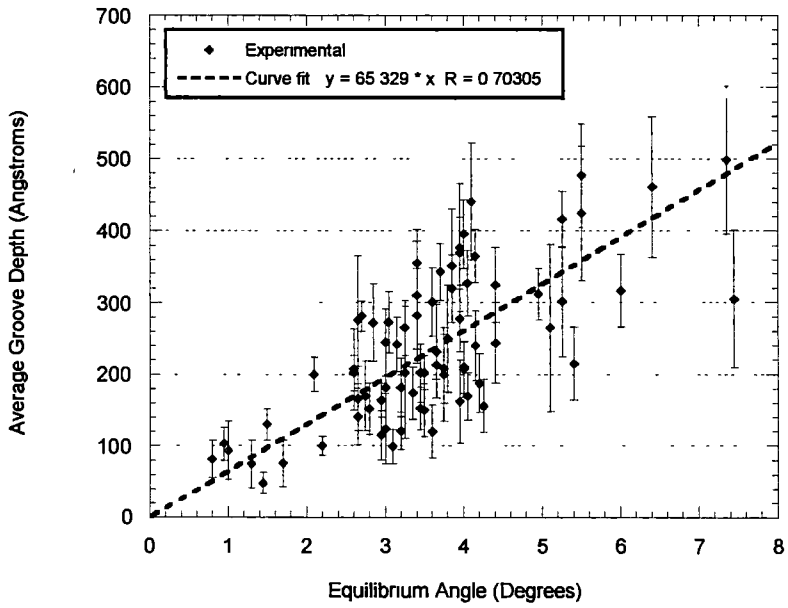

(b) Annealed at 800°C, 30 min.

Figure 4.8. Average depth of thermal grooves as a function of equilibrium angle for cube-textured nickel. Error bars indicate the standard deviation about the mean for each data point.

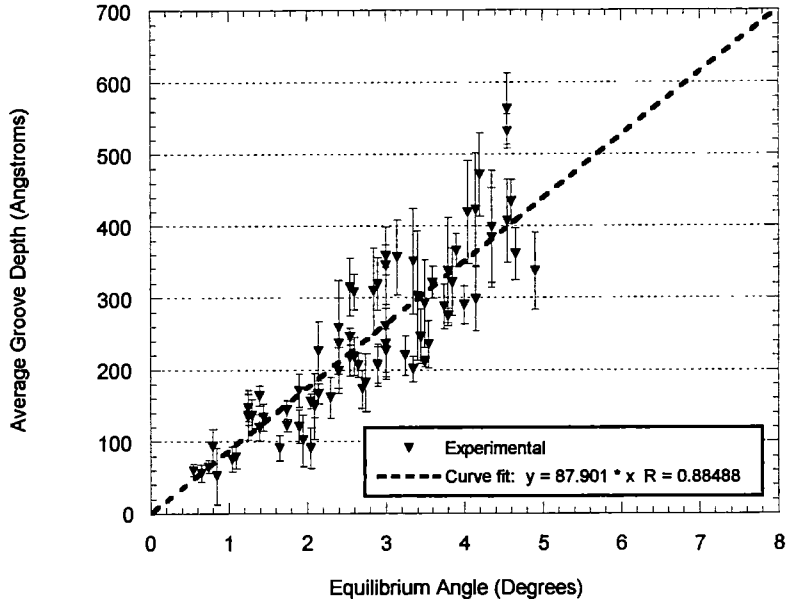

(c) Annealed at 800°C, 1 hr.

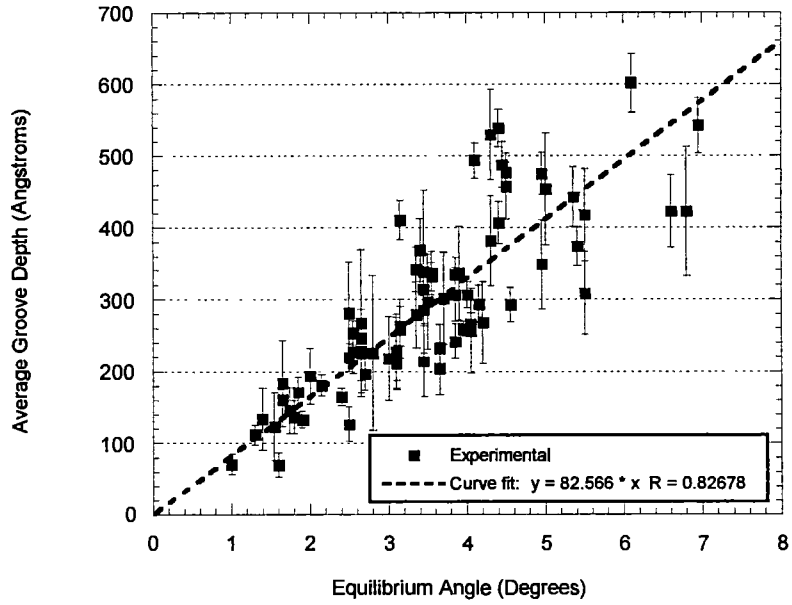

(d) Annealed at 800°C, 2 hrs.

Figure 4.8. (continued)

grain-boundary energy increases with increasing equilibrium angle in the range $0° \leq \alpha \leq 90°$, grooves with larger equilibrium angles grow more rapidly. Thus, the slope of the line fit must increase with time. Scatter in the data due to uncertainties associated with calculating mean groove depths and experimental errors may account for the decrease in the slope of the line fit in Figure 4.8 (d). Experimental errors and uncertainties related to AFM measurements are discussed in the Appendix.

The relationship between groove growth rate and the slope m (or the equilibrium angle α) can be obtained in a simple manner. By differentiating Equation 2.3 with respect to time, the instantaneous growth rate d' (cm/s) of a diffusion-induced thermal groove is given as follows:

$$d' = 0.243 m B^{\frac{1}{4}} t^{-\frac{3}{4}} \tag{4.3}$$

From Equation 4.3, it is apparent that an increase in the slope m will increase the rate of grooving if B and t are constants. Figure 4.9 is a plot of calculated, instantaneous growth rates at 800°C as a function of m and as a function of α for t = 600, 1800, 3600, and 7200 seconds and $B = 4.53 \times 10^{-22}$ $cm^4 s^{-1}$. The magnitude of B was estimated by using the results of the curve fit in Figure 4.6 and Equations 2.6 and 4.1.

4.4 Effect of Absolute Misorientation Angle on Groove Depth

Several AFM scans, EBSD patterns, and SEM images were examined in order to determine if absolute misorientation angle would affect the final depth of a groove formed during high temperature annealing. The SEM images (Figure 4.10) were used to match the indexed EBSD patterns with the grains from which they were collected. Then, they

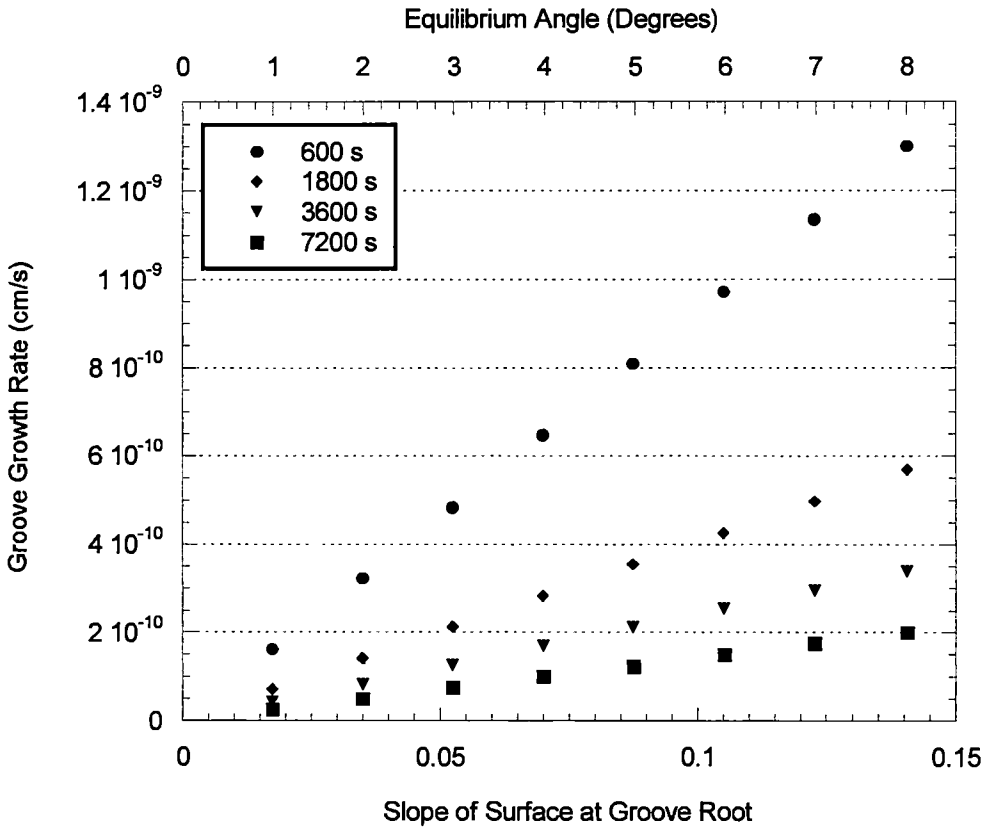

Figure 4.9. Instantaneous growth rates of thermal grooves for four times at 800°C as a function of slope m and equilibrium angle α. $B = 4.53 \times 10^{-22}$ cm^4s^{-1}.

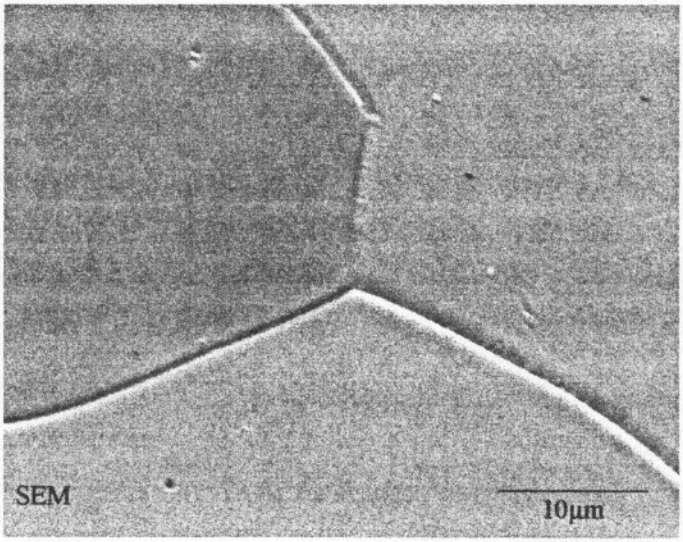

Figure 4.10. SEM image of the triple point shown in Figure 4.1. Images like this were used to match EBSD patterns with Ni grains. This image is rotated clockwise 90° with respect to the 2-D image in Figure 4.1 (a).

were matched with their corresponding AFM scans, which were used to measure groove depth. The absolute orientations of grains were determined from the indexed patterns, and Bollman's theory[4,34] was used to calculate absolute misorientation angles between grains. The misorientation angles were then related to the corresponding groove depths.

Figures 4.11 (a, b, c, and d) are plots of average groove depth versus absolute misorientation angle ($\leq 15°$) for Ni samples annealed at 800°C for 10, 30, 60, and 120 minutes. The data in these plots may appear to be randomly scattered, but there seems to be a tendency for the average groove depth to increase with increasing absolute misorientation angle. The large scatter in the data may be due to an inability of absolute misorientation angle to accurately represent the energy associated with any specific grain-boundary in the low angle regime. For example, the orientation of the grain-boundary plane relative to two adjoining crystals can affect the grain-boundary energy independently of the absolute misorientation angle. Therefore, it may be necessary to use another measurement of the grain misorientation to completely describe the grain-boundary energy associated with a thermal groove.

Another interesting observation is that there is also no apparent reduction in the scatter of the data in Figure 4.11 with increasing annealing time. This may indicate, in general, that grain-boundary planes move into their lowest energy configuration in a short time during annealing. Thus, their effect on grain boundary energy is fairly constant with time, and there is always an energy contribution due to grain-boundary plane orientation to the total grain-boundary energy.

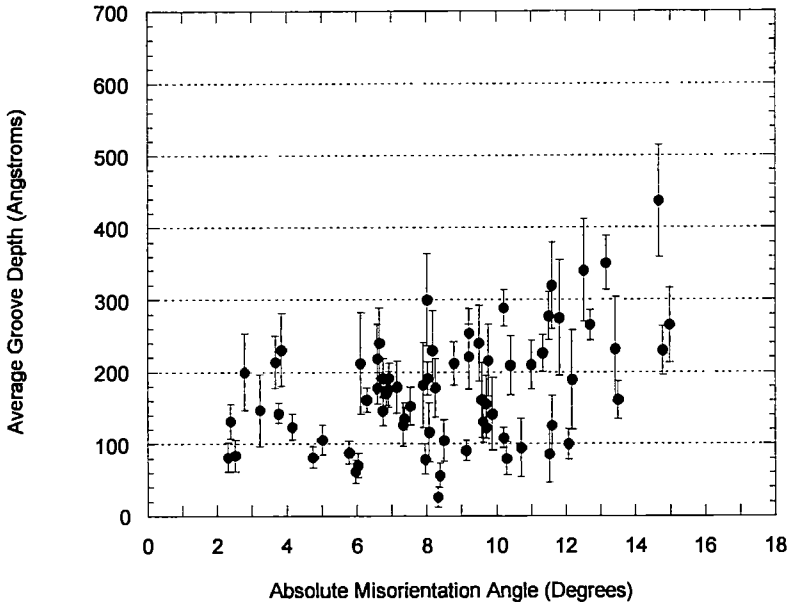

(a) Annealed 800°C, 10 min.

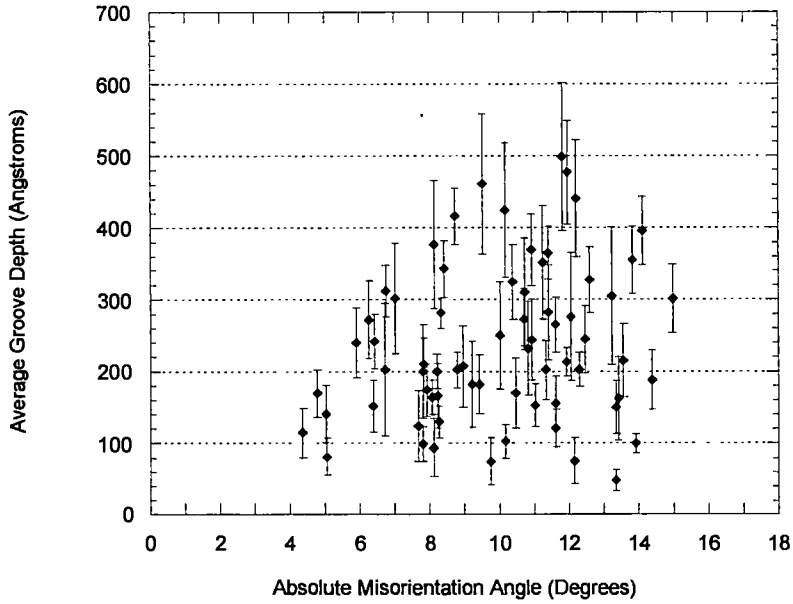

(b) Annealed at 800°C, 30 min.

Figure 4.11 Plots of average groove depth versus absolute misorientation angle for cube-textured nickel. Error bars indicate standard deviation about the mean.

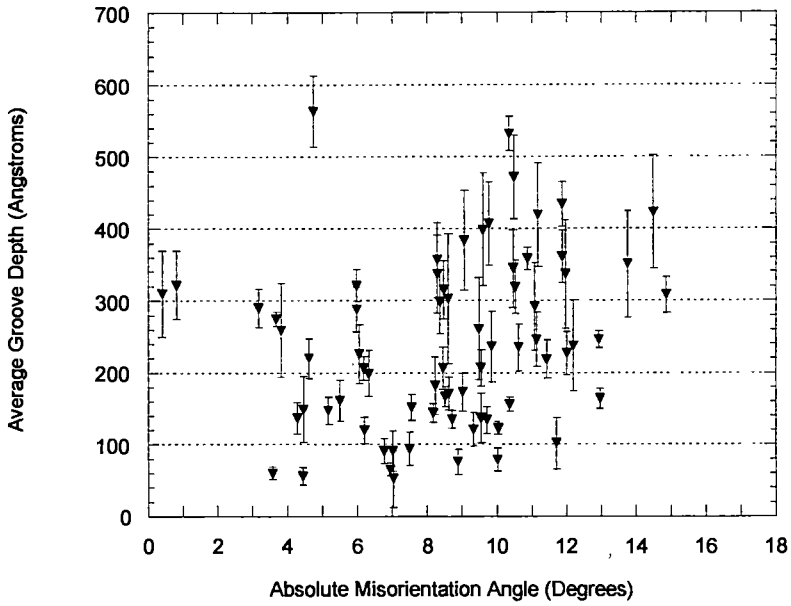

(c) Annealed at 800°C, 1hr.

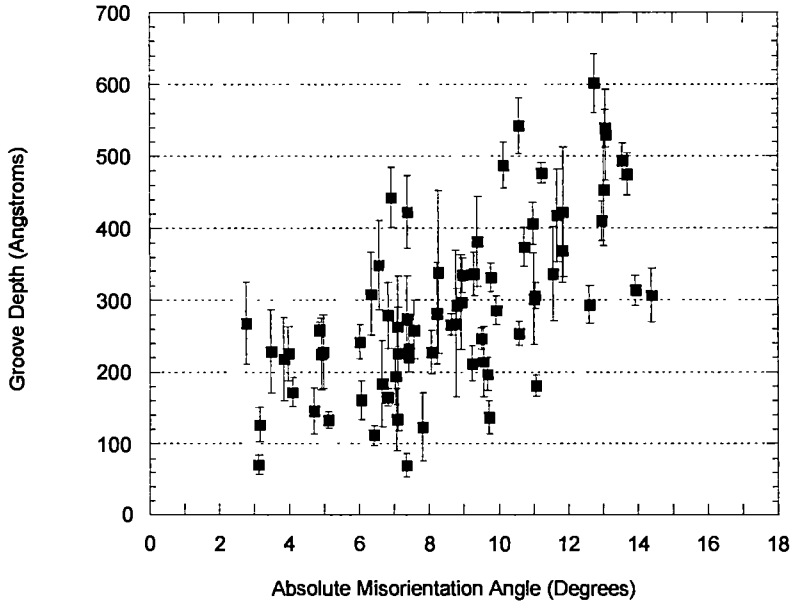

(d) Annealed at 800°C, 2hrs.

Figure 4.11. (continued)

4.5 Texture Analysis

X-ray diffraction was used to produce (111) pole figures for the Ni samples studied in this experiment. This was necessary to confirm that the cube texture in each Ni sample was well developed and to ensure that AFM and EBSD data had been collected from typical specimens of RABiTS Ni. The (111) x-ray pole figures for the Ni specimens annealed at 800°C for 10, 30 ,60, and 120 minutes are shown in Figure 4.12 (a, b, c, and d). As can be seen, the cube texture, which is defined by the sharpness and intensity of the four (111) peaks, is very well developed in each sample. Any large deviation from the desired cube texture would be manifested in the pole figures as a severe broadening of the (111) peaks. For a single crystal of Ni, a (111) pole figure would consist only of four highly intense (111) spots. The slight broadening of the (111) peaks in Figure 4.12 is due to small, in-plane and out-of-plane, grain misalignments. The low intensity regions surrounding the peaks are thought to be caused by the random reflection of x-rays off of the sample stage used to oscillate the specimen through the x-ray beam.

4.6 Grain Size and Growth

The grain size of each Ni sample was measured to confirm that it was in fair agreement with the average grain size of 50-100 μm reported by Goyal *et al.*[5] for RABiTS Ni recrystallized at 1000°C for 4 hrs. The results of the measurements are listed in Table 4.1, and Figure 4.13 shows optical photomicrographs of the grain structures of samples after recrystallization. As can be seen, the grain sizes measured in this study are at the bottom end of the reported range, possibly due to the lower annealing temperature. Also,

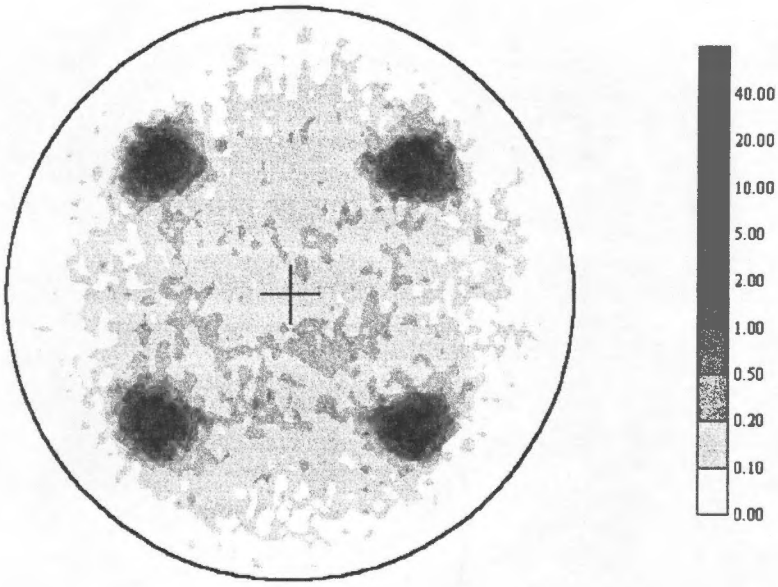

(a) Annealed at 800°C, 10 min.

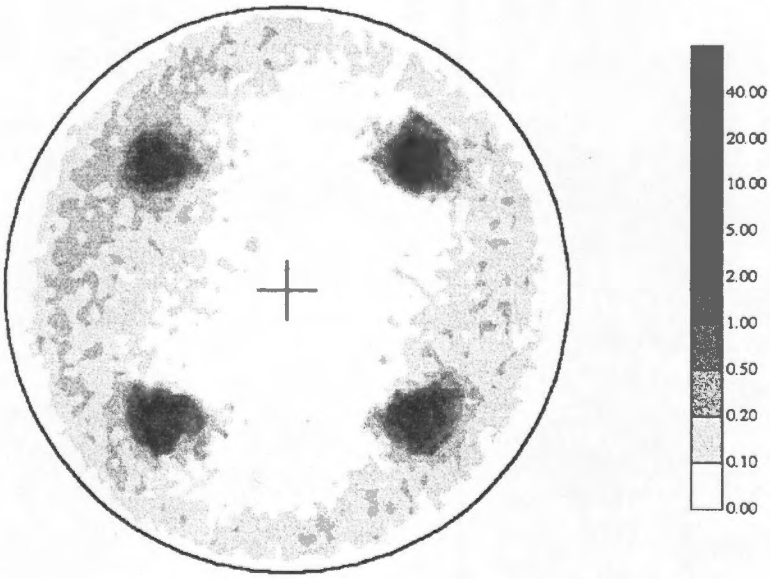

(b) Annealed at 800°C, 30 min.

Figure 4.12. (111) x-ray diffraction pole figures for RABiTS nickel after recrystallization, indicating the presence of a sharp {100}⟨001⟩ cube texture.

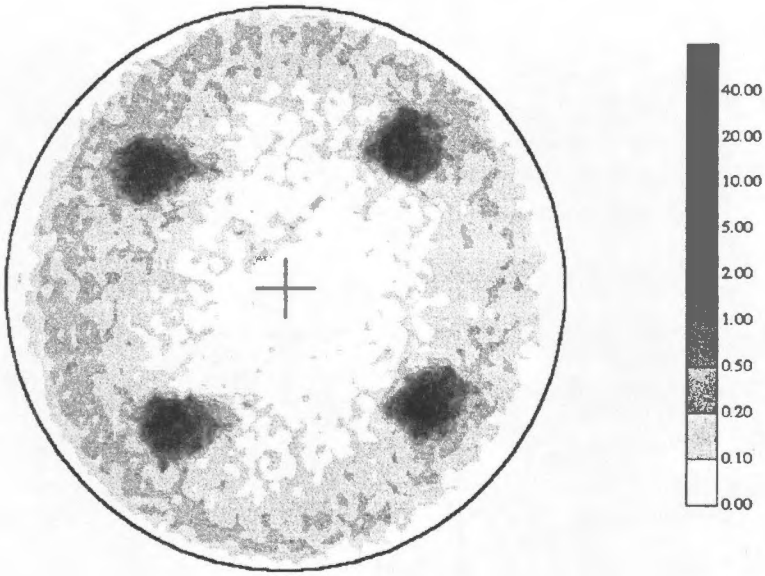

(c) Annealed at 800°C, 1hr.

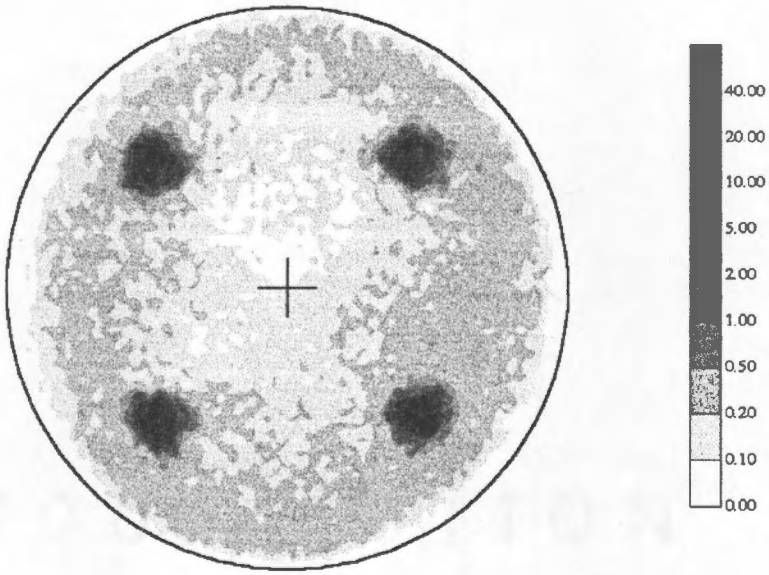

(d) Annealed at 800°C, 2hrs.

Figure 4.12. (continued)

Table 4.1. Grain size measurement data for RABiTS Ni samples after recrystallization.

Annealing Time (minutes)	Annealing Temperature (°C)	Mean Value of the Mean Lineal Intercept (mm)	Percent Relative Accuracy	Average Grain Diameter (mm)
10	800	0.0394	8.47	0.0443
30	800	0.0416	3.32	0.0468
60	800	0.0462	6.25	0.0519
120	800	0.0474	5.89	0.0533

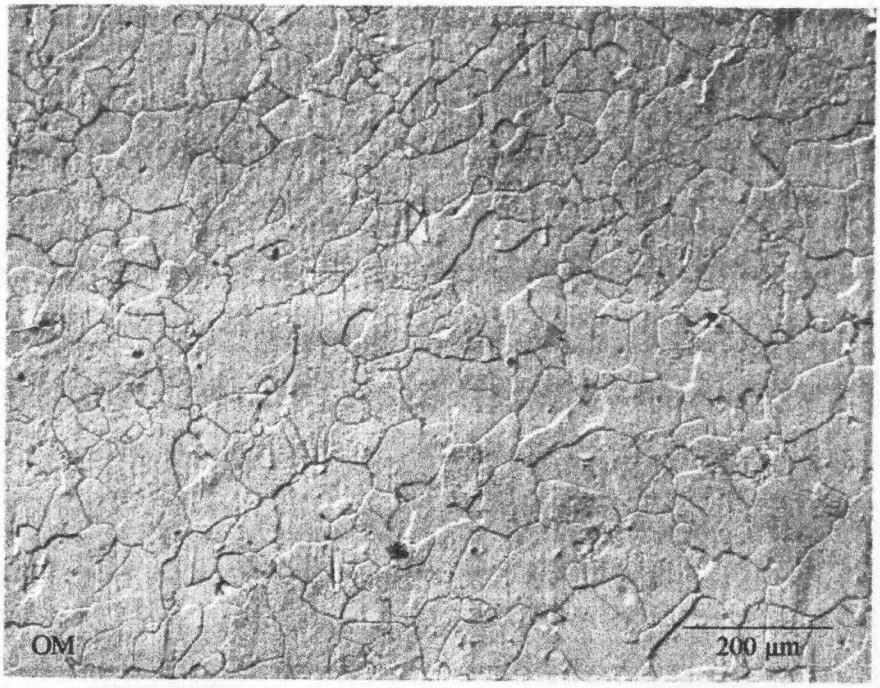

(a) Annealed at 800°C, 10 min. Average grain diameter d_{avg} = 0.0443 mm.

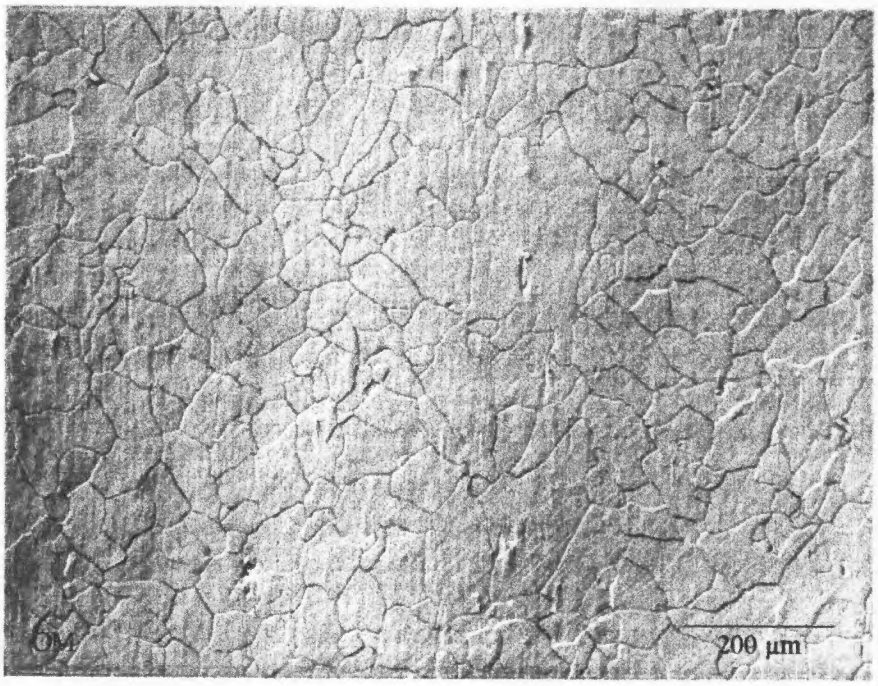

(b) Annealed at 800°C, 30min. Average grain diameter d_{avg} = 0.0468 mm.

Figure 4.13 Photomicrographs of the grain structure of RABiTS Ni samples after recrystallization. Samples were etched with glyceregia for 90 seconds.

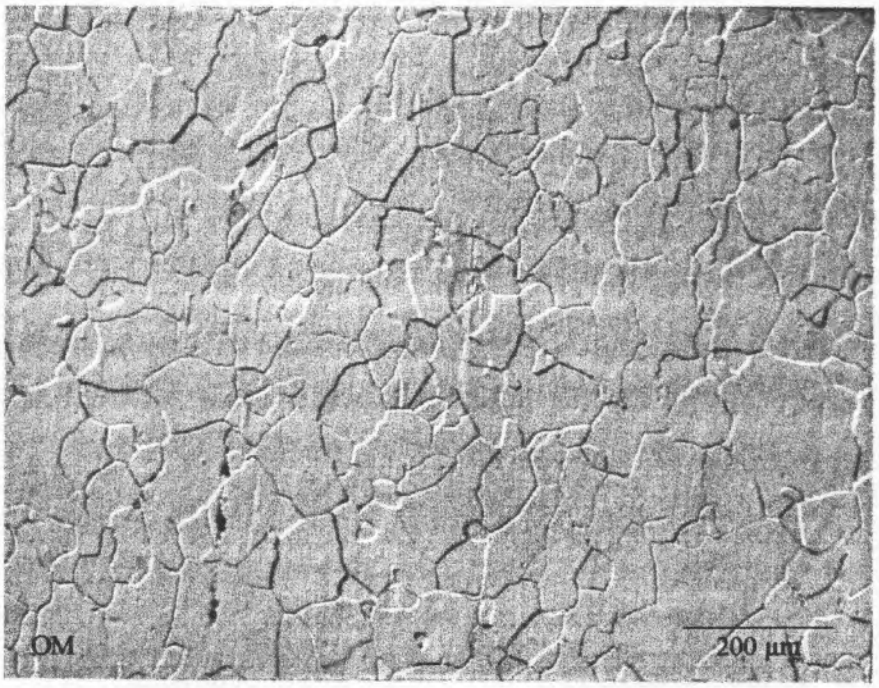

(c) Annealed at 800°C, 1 hr. Average grain diameter d_{avg} = 0.0519 mm.

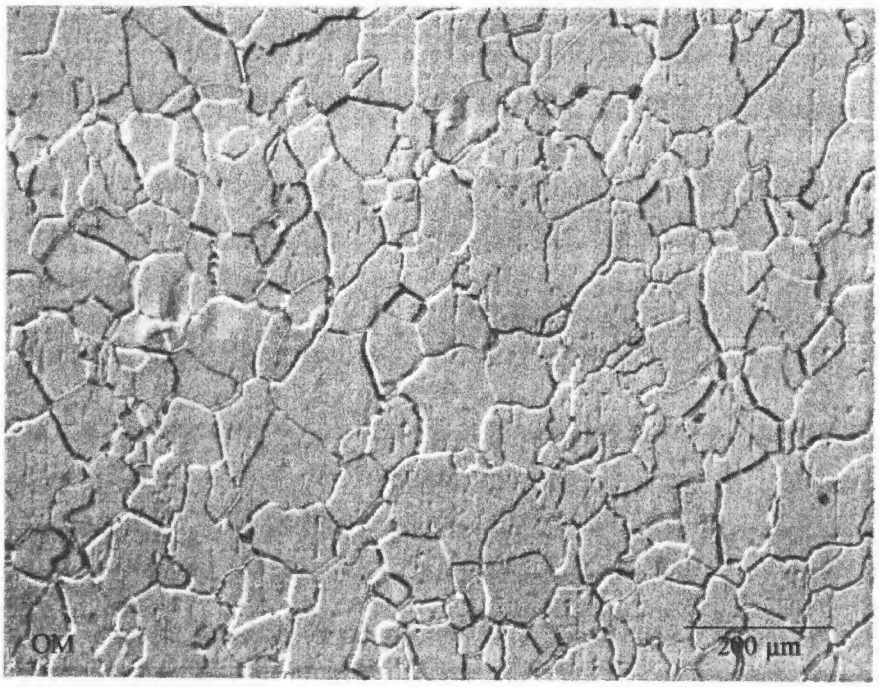

(d) Annealed at 800°C, 2hrs. Average grain diameter d_{avg} = 0.0533 mm.

Figure 4.13 (continued)

the tabulated data show that average grain size does not increase significantly with increasing annealing time beyond 10 minutes. In the first 10 minutes of recrystallization, growth was extremely rapid, and grains grew from very small nuclei to an average diameter of approximately 44 μm.

If a polycrystalline metal, such as the Ni used to prepare samples in this study, is cold rolled to greater than 90% reduction, a rolling texture develops in the material.[32] Upon recrystallization at high temperature, new grains nucleate and grow with a preferred orientation. These grains have higher mobility grain boundaries and grow faster than grains with no preferred orientation. Thus, they will consume the randomly oriented grains, and a recrystallization texture will develop.[32] If, however, the consumption of highly misoriented grains is slowed due to grain-boundary pinning by thermal grooves, the cube texture of a specimen may be adversely affected. It is difficult to conclusively determine if grain growth in RABiTS Ni is significantly slowed by grain-boundary grooving.

CHAPTER 5

CONCLUSIONS

The effects of annealing time, equilibrium angle, and absolute misorientation angle on thermal grain-boundary grooving in cube-textured nickel have been investigated. This study has revealed that Mullins' theory adequately describes the thermal grooving phenomenon in RABiTS nickel. Thus, his theory may be used to predict the time-dependent growth behavior of thermal grooves. Also, Mullins' theory shows how the equilibrium angle of a groove can affect its growth. Concerning absolute misorientation angle, its effect on grooving is difficult to determine because of other factors which affect the grain-boundary energy. The specific conclusions developed from this work are as follows:

1. Thermal grain-boundary grooves form in abundance on RABiTS Ni samples annealed at or above 800°C. These grooves can occur in two morphologies: diffusion-induced and faceted. The groove morphology depends on the conditions of annealing, specifically the annealing temperature and the local annealing atmosphere.

2. On average, the dimensions of diffusion-induced, thermal grain-boundary grooves on RABiTS Ni samples increase with time in accordance with Mullins' theory of groove formation and growth by surface diffusion. Thus, the initial growth rate of thermal grooves is very rapid with the rate decreasing with increasing annealing time.

3. Generally, the thermal grooves in RABiTS Ni have very small dimensions with depths no larger than 650 Å and widths no larger than 2.5 μm after 2hrs. of annealing at 800°C in vacuum. However, some deep grooves (≥ 1500 Å) were observed surrounding small grains (10-20 μm).

4. From AFM measurements, it was determined that the average depth of thermal grain-boundary grooves increases with increasing equilibrium angle in the small-slope regime. Also, the rate of grooving increases with increasing equilibrium angle. Equilibrium angle has no measurable effect on groove width.

5. A strong relationship does not exist between absolute misorientation angle and grain-boundary groove depth; however, there seems to be a tendency for groove depth to increase with increasing misorientation angle. The lack of a strong correlation may be due to the effect of grain-boundary plane orientation on grain-boundary energy.

6. The grain size and degree of cube texture of the RABiTS Ni samples examined in this experiment are consistent with results reported by Goyal *et al.*[6]

7. Although grain-boundary grooves in RABiTS Ni were observed to have a high ratio of width to depth (30 - 40:1) and do not appear to be a serious mechanical flaw, they may still cause growth defects to form in subsequently deposited layers of a RABiT substrate. These growth defects could create mechanical weaknesses in the oxide layers which may rupture under stress.

8. Using the data collected in this study, more research is necessary to determine if grain-boundary grooves in RABiTS Ni can behave as initiation sites for cracks in the oxide layers (buffer and superconductor) under specific types of mechanical loading.

9. Because thermal grooves are formed as a result of a surface effect, it may be possible to stop their formation by altering the surface condition of the material. For example, the Ni could be recrystallized at low temperature to form the cube-texture. At 400-500°C, no significant grooves would form. Then the sample could be coated with an oxide buffer layer and annealed at high temperature to bring grain growth to an effective termination. This final anneal would also refine the cube-texture.

As mentioned previously, grain-boundary grooves do not seem to be severe mechanical defects because of their subtle geometry, but they should not be dismissed because other serious flaws may form as a result of their presence. The information presented in this thesis is intended to provide a basis for further work in which the effects of thermal grooves on the performance of layered conductors are modeled or experimentally determined.

LIST OF REFERENCES

1. V. Z. Kresin and S. A. Wolf, *Fundamentals of Superconductivity* (Plenum Press NewYork, 1990).

2. T. P. Sheahan, *Introduction to High-Temperature Superconductivity* (Plenum Press, New York, 1994).

3. C. Krause, *ORNL Review* **29**, 4 (1996).

4. A. Goyal, E. D. Specht, Z. L. Wang, and D. M. Kroeger, *Ultramicroscopy* **67**, 35 (1997).

5. A. Goyal, D. P. Norton, D. M. Kroeger, D. K. Christen, M. Paranthaman, E. D. Specht, J. D. Budai, Q. He, B. Saffian, F. A. List, D. F. Lee, E. Hatfield, P. M. Martin, C. E. Klabunde, J. Mathis, and C. Park, *J. Mater. Res.* **12**, 2924 (1997).

6. A. Goyal, D. P. Norton, D. K. Christen, E. D. Specht, M. Paranthaman, D. M. Kroeger, J. D. Budai, Q. He, F. A. List, R. Feenstra, H. R. Kerchner, D. F. Lee, E. Hatfield, P. M. Martin, J. Mathis, and C. Park, *Appl. Supercond.* **4**, 403 (1998).

7. A. Goyal, D. P. Norton, J. D. Budai, M. Paranthaman, E. D. Specht, D. M. Kroeger, D. K. Christen, Q. He, B. Saffian, F. A. List, D. F. Lee, P. M. Martin, C. E. Klabunde, E. Hatfield, and V. K. Sikka, *Appl. Phys. Lett.* **69**, 1795 (1996).

8. A. Goyal, D. P. Norton, M. Paranthaman, J. D. Budai, E. D. Specht, D. K. Christen, D. M. Kroeger, Q. He, B. Saffian, F. A. List, D. F. Lee, C. E. Klabunde, and P. M. Martin, *Proceedings of the 9th International Symposium on Superconductivity*, Sapporo, Japan, (1996).

9. M. Paranthaman, A. Goyal, D. P. Norton, F. A. List, E. D. Specht, D. K. Christen, D. M. Kroeger, J. D. Budai, Q. He, B. Saffian, D. F. Lee, and P. M. Martin, *Proceedings of the 9th International Symposium on Superconductivity*, Sapporo, Japan, (1996).

10. G. E. Dieter, *Mechanical Metallurgy, 3rd ed.* (McGraw-Hill, New York, 1986).

11. W. F. Smith, *Principles of Materials Science and Engineering, 2nd ed.* (McGraw-Hill, New York, 1990).

12. D. M. Kroeger and A. Goyal, *JOM* **46**,14 (1994).

13. A. Goyal, E. D. Specht, D. M. Kroeger, T. A. Mason, D. J. Dingley, G. N. Riley, and M. W. Rupich, *Appl. Phys. Lett.* **66**, 2903 (1995).

14. E. D. Specht, A. Goyal, and D. M. Kroeger, *Phys. Rev. B* **53**, 3585 (1996).

15. D. F. Lee (private communication).

16. D. Dimos, P. Chaudhari, J. Mannhart, and F. K. LeGoues, *Phys. Rev. Lett.* **61**, 219 (1988).

17. Y. Iijima, N. Tanabe, O. Kohno, and Y. Ikeno, *Appl. Phys. Lett.* **60**, 769 (1992).

18. Y. Iijima, K. Onabe, N. Futaki, N. Sadakata, O. Kohno, and Y. Ikeno, *J. Appl. Phys. Lett.* **74**, 1905 (1993).

19. M. Paranthaman, A. Goyal, F. A. List, E. D. Specht, D. F. Lee, P. M. Martin, Q. He, D. K. Christen, D. P. Norton, J. D. Budai, and D. M. Kroeger, *Physica C* **275**, 266 (1997).

20. F. A List, A. Goyal, M. Paranthaman, D. P. Norton, E. D. Specht, D. F. Lee, and D. M. Kroeger, *Physica C* **302**, 87 (1998).

21. H. Makita, S. Hanada, and O. Izumi, *Acta. Met.* **36**, 403 (1988).

22. A. Merlini and P. A. Beck, *Acta Met.* **1**, 598 (1953).

23. H. Hu, *Scripta Met.* **19**, 1471 (1985).

24. H.-J. Bunge, *Texture Analysis in Materials Science: Mathematical Methods* (Butterworths, London, 1982).

25. W. W. Mullins, *J. Appl. Phys.* **28**, 333 (1957).

26. W. W. Mullins, *Acta. Met.* **6**, 414 (1958).

27. R. E. Read-Hill, *Physical Metallurgy Principles, 2nd ed.* (D. Van Nostrand Co., New York, 1973).

28. L. E. Murr, *Interfacial Phenomena in Metals and Alloys* (Addison-Wesley, Reading, MA, 1975).

29. N. A. Gjostein and F. N. Rhines, *Acta Met.* **7**, 319 (1959).

30. W. Zhang and J. H. Schneibel, *Comp. Mater. Sci.* **3**, 347 (1995).

31. W. M. Robertson, *J. Appl. Phys.* **42**, 463 (1970).

32. D. A. Porter and K. E. Easterling, *Phase Transformations in Metals and Alloys, 2nd ed.* (Chapman & Hall, London, 1992).

33. H.-J. Bunge, in *Perferred Orientation in Deformed Metals and Rocks: An Introduction to Modern Texture Analysis*, edited by H. R. Wenk (Academic, Orlando, FL, 1985), p. 73.

34. W. Bollman, in *Crystal Lattices, Interfaces and Matrices* (published by author, 1982).

35. A. Goyal, E. D. Specht, D. M. Kroeger, and T. A. Mason, *Appl. Phys. Lett.* **68**, 711 (1996).

36. Park Scientific Instruments, *User's Guide to Autoprobe LS*, Sunnyvale, CA (1993).

37. B. Mantiply, (private communication).

38. G. F. Vander Voort, *Metallography: Principles and Practice* (McGraw-Hill, New York, 1984).

APPENDIX

EXPERIMENTAL ERROR

In this experiment a very large number of linear measurements were made with an atomic force microscope, and several calculations were performed using the data from these measurements. The sources and effects of systematic and random experimental errors on these measurements are considered.

Sources of systematic error in atomic force microscope measurements may be instrumental electrical noise, probe tip diameter and geometry effects, and faulty calibration of the piezoelectric scanner response. Care was taken to reduce each of these sources of systematic error. Electrical noise was controlled by performing a noise test each time a tip was replaced. Tips which produced more than 5 Å rms noise were discarded. Measurement errors due to tip diameter and geometry are more difficult to quantify and correct because the tip wears with use. Thus, its diameter and geometry at any given time are unknown. The only practical method of controlling error due to tip effects was to change the tip periodically. Also, if an obviously distorted image was produced by the AFM, the tip was changed. Unfortunately, a tip deconvolution algorithm, like that developed by Markiewicz and Goh,[A1,A2] was not available for the Auto Probe XL AFM at the onset of this experiment. To reduce error due to the response of the piezoelectric scanner, it was calibrated with measurement standards. Also, a calibration curve was generated for the *z*-piezo response so that corrections could be applied to the data if necessary.

Concerning the effects of systematic errors on AFM measurements, sinusoidal electrical noise would cause periodic distortions in the fast-scan direction of the AFM image and create a maximum error in *z*-height measurements of plus or minus the value of

the amplitude of the noise. Tip diameter can affect the depth measurements of grooves as shown in Figure A.1. Because the tip diameter is finite (diameter of new tip ≈ 20 nm), it cannot reach the absolute minima of a grain boundary groove. Thus, it will yield a measurement which is less than the true depth of the groove. Also, as the equilibrium angle of the groove increases, the effect causes the error to become more severe. The effect of faulty calibration of the AFM scanner would simply be to offset the measurement values.

For this experiment, examples of random errors are measurement fluctuations because of human error, sudden changes in the AFM probe tip diameter or geometry (i.e. the tip accumulates debris, water, etc.), and random fluctuations of groove dimensions and geometry along the groove length which create uncertainty in mean values of depth, width, and equilibrium angle. Measurement fluctuations were minimized by carefully identifying the maxima and minima between which groove measurements were made. As with systematic error caused by tip effects, those caused by random changes in tip diameter and geometry are difficult to quantify and reduce. To help keep such errors to a minimum, only very clean samples were examined, and the humidity in the AFM laboratory was monitored and controlled. Uncertainty in mean groove depth and width as a result of random fluctuations in groove dimensions can be minimized by performing more measurements and reducing the standard deviation from the mean. Unfortunately, the number of measurements needed to do this was prohibitively large.

The effect of all random errors is to create scatter in the data collected. Scatter in the data due to human error and sudden changes in the probe tip diameter and

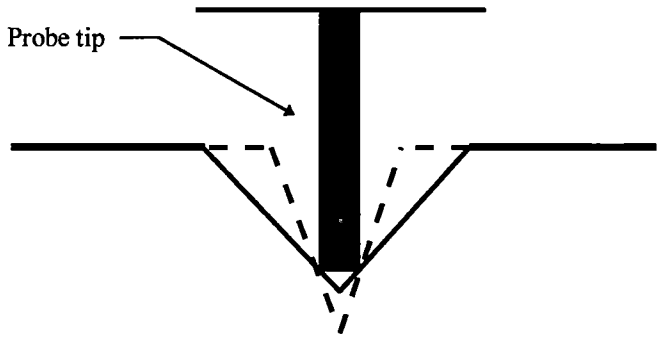

Figure A.1. Schematic diagram of measurement error due to the finite diameter of an AFM probe tip. The error in the measurement of depth is greater for a groove with a large equilibrium angle (dashed line) than for one with a small equilibrium angle (solid line).

geometry is thought to be small. However, scatter due to sudden, random fluctuations in groove dimensions is thought to fairly significant. In some cases, the standard deviation from the mean depth of a groove was found to be greater than 100 Å. An uncertainty of this magnitude indicates that the depth measurements may be very imprecise and that the histograms in Figures 4.5 may not be good representations of the distributions of groove depths. Likewise, similar uncertainties in the mean widths of grooves indicate that the histograms in Figure 4.4 may not be experimentally reproducible.

LIST OF REFERENCES - APPENDIX

A1. P. Markiewicz and M. C. Goh, *Langmuir* **10**, 5 (1994).

A2. P. Markiewicz and M. C. Goh, *Rev. Sci. Instrum.* **66**, 3186 (1995).

VITA

Conrad Joseph Simon, III was born on September 18, 1970 in San Diego, California. His family moved to Pittsburgh, Pennsylvania in 1971 and to Richmond, Virginia in 1973. He attended elementary school in the latter city and later in Longwood, Florida and Germantown, Tennessee. After graduating from Germantown High School in 1988, he entered The University of Tennessee, Knoxville and earned a Bachelor of Science degree in Materials Science and Engineering in December 1994. Following graduation, he accepted a full-time engineering position with British Tire and Rubber. In August 1996, he returned to academia as a graduate research assistant at The University of Tennessee Space Institute and began study toward a Master of Science degree in Metallurgical Engineering. He received the degree in May 1999.